

See discussions, stats, and author profiles for this publication at: <https://www.researchgate.net/publication/319271470>

Precise and fast computation of gravitational field of general finite body and its application to gravitational study of asteroid Eros (3rd rev)

Technical Report · August 2017

CITATIONS

0

READS

208

1 author:



[Toshio Fukushima](#)

National Astronomical Observatory of Japan

755 PUBLICATIONS 3,134 CITATIONS

[SEE PROFILE](#)

Some of the authors of this publication are also working on these related projects:



Report on IAU/IAG/IERS Activities [View project](#)



Computation of General Integrals of Fermi-Dirac/Bose-Einstein Distribution [View project](#)

PRECISE AND FAST COMPUTATION OF GRAVITATIONAL FIELD OF GENERAL FINITE BODY AND ITS APPLICATION TO GRAVITATIONAL STUDY OF ASTEROID EROS

TOSHIO FUKUSHIMA¹

¹*National Astronomical Observatory / SOKENDAI, Ohsawa, Mitaka, Tokyo 181-8588, Japan*

(Received; Revised; Accepted)

Submitted to AJ

ABSTRACT

In order to obtain the gravitational field of a general finite body inside its Brillouin sphere, we developed a new method to compute the field accurately. First, the body is assumed to consist of some layers in a certain spherical polar coordinate system and the volume mass density of each layer is expanded as a Maclaurin series of the radial coordinate. Second, the line integral with respect to the radial coordinate is analytically evaluated in a closed form. Third, the resulting surface integrals are numerically integrated by the split quadrature method using the double exponential rule. Finally, the associated gravitational acceleration vector is obtained by numerically differentiating the numerically integrated potential. Numerical experiments confirmed that the new method is capable of computing the gravitational field independently of the location of the evaluation point, namely whether inside, on the surface of, or outside the body. Also, it can provide sufficiently precise field values, say of 14–15 digits for the potential and of 9–10 digits for the acceleration, respectively. Furthermore, its computational efficiency is better than that of the polyhedron approximation. This is because the computational error of the new method decreases much faster than that of the polyhedron models when the number of required transcendental function calls increases. As an application, we obtained the gravitational field of 433 Eros from its shape model expressed as the 24×24 spherical harmonic expansion by assuming the homogeneity of the object.

Keywords: asteroid: 433 Eros – celestial mechanics – gravitation –
methods: numerical

1. INTRODUCTION

Spurred by the achievement of the asteroid explorer HAYABUSA (Fujiwara et al. 2006), the JAXA launched its successor, HAYABUSA2, on Dec. 3, 2014. It is scheduled to land on the asteroid 162173 Ryugu in June–July 2018 (Tsuda et al. 2013). In order to assist the descending orbit design of the spacecraft and its probe MAS-COT (Matsuoka and Russell 2017), we started an investigation to compute accurately the gravitational field of Ryugu when its detailed information will be available (Müller et al. 2017).

Of course, the computation of the gravitational field of a general object is a classic problem in astronomy and geodesy from the days of Newton (Heiskanen and Moritz 1967; Binney and Tremaine 2008). However, analytical solutions are known only for a limited type of objects (Chapman 1979; Heck and Seitz 2007; Wild-Pfeiffer 2008): (i) a general spherically symmetric object shown by Newton himself (Chandrasekhar 1995) and a homoeoid as its ellipsoidal generalization (Chandrasekhar 1969), (ii) a homogeneous body with simple shapes such as an infinitely fine straight line segment (Kellogg 1929, Chapter 3, Sect. 3, Excurs. 1), an infinitely thin rectangle (Fukushima 2016b), a rectangular parallelepiped (MacMillan 1930), a polyhedron as its generalization (Paul 1974), an infinitely fine circular ring (Kellogg 1929, Chapter 3, Sect. 4), an infinitely thin circular disc (Fukushima 2010), and a triaxial ellipsoid (Byrd & Friedman 1971, Introduction, Example III), and (iii) an inhomogeneous case as a polyhedron with a density distribution described by a linear function and low degree polynomials (Garcia-Abdeslem 1992).

Consequently, for a general volume mass density distribution of the object, $\rho(\mathbf{x})$, a possible approach to obtain its gravitational field is the numerical quadrature of the following types (Laplace 1799):

$$V(\mathbf{X}) \equiv G \int \frac{\rho(\mathbf{x})}{|\mathbf{x} - \mathbf{X}|} d^3x, \quad (1)$$

$$\mathbf{a}(\mathbf{X}) \equiv \frac{\partial V}{\partial \mathbf{X}} = G \int \frac{\rho(\mathbf{x}) (\mathbf{x} - \mathbf{X})}{|\mathbf{x} - \mathbf{X}|^3} d^3\mathbf{x}, \quad (2)$$

where G is Newton’s gravitational constant, \mathbf{X} is the point of evaluation, \mathbf{x} is the point of an internal mass element, $V(\mathbf{X})$ is the negative gravitational potential, and $\mathbf{a}(\mathbf{X})$ is the gravitational acceleration vector. Nevertheless, the kernel functions of these convolution integrals contain algebraic singularities of order 1 and 2. As a result, their proper integration had been difficult (Klees and Lehmann 1998).

If the object is finite, on the other hand, $V(\mathbf{X})$ satisfies the Laplace equation outside the object. As a result, $V(\mathbf{X})$ can be expanded as an infinite series of basis functions satisfying the Laplace equation in some selected coordinate systems (Hobson 1931). In this case, an issue to be resolved is the precise and fast computation of the basis functions termed the harmonics for arbitrary combination of their indices, parameters, and/or arguments. In the last couple of decades, this problem has been positively

solved: the spherical harmonics (Fukushima 2012a,b,c, 2014c), the oblate spheroidal harmonics (Fukushima 2013), the prolate spheroidal harmonics (Fukushima 2014a), the triaxially ellipsoidal harmonics (Garmier and Barriot 2001, 2002), and the axisymmetric toroidal harmonics (Fukushima 2016c). For instance, high degree/order spheroidal harmonic expansions are successfully determined for asteroids Bennu and Castalia (Sebera et al. 2016).

However, we warn the readers that, even outside the object, the harmonic expansions do not always converge uniformly (Moritz 1980). The domain of the convergence is called the Brillouin manifold (Jekeli 2007). Refer to Fig. 1 illustrating its spherical example, the Brillouin sphere. If the shape of the object is as complicated as that of asteroid Itokawa (Müller et al. 2014), the domain inside the Brillouin manifold but outside the object is not negligibly small. Thus, problematic are the attempts to utilize the harmonic expansions only in evaluating the external gravitational field of such objects, especially in designing the descending orbit of a space probe such as HAYABUSA2/MASCOT (Watanabe et al. 2017).

Actually, there exist trials to represent the solution in the outside of the object as a combination of not the external but the internal harmonic expansions around different coordinate centers (Takahashi et al. 2013). **Also, recently proposed is the internal/external series expansions using the spherical Bessel functions (Takahashi and Scheeres 2014).** Among these, recommended was the **conditional switch of multiple internal harmonic expansions with different coordinate centers** (Takahashi and Scheeres 2014). None the less, its realization is cumbersome if one wants to cover all the exterior domain of irregular shaped objects such as asteroid Eros (Zuber et al. 2000).

This is the reason why the polyhedron models have been widely adopted in computing the gravitational field of asteroids, comets, and small satellites (Scheeres 1994; Werner and Scheeres 1997; Miller et al. 2002; Thomas et al. 2002; Hikida and Wieczorek 2007; Konopliv et al. 2014; Park et al. 2014; Zhao et al. 2016; Lhotka et al. 2016; Aljbaae et al. 2017). In fact, they are frequently used in the dynamical study of orbits around such objects (Scheeres et al. 1996, 1998; Rossi et al. 1999; Scheeres et al. 2000; Hu and Scheeres 2004, 2008; Yu and Baoyin 2012a,b, 2013, 2015; Li et al. 2013; Chanut et al. 2014; Wang et al. 2014; Chanut et al. 2015b; Jiang and Baoyin 2016; Wang et al. 2016; Li et al. 2017). This popularity is supported by a number of theoretical and computational developments in the polyhedron models (Nagy 1966; Barnett 1976; Okabe 1979; Waldvogel 1979; Pohanka 1988; Werner 1994; Holstein and Ketteridge 1996; Petrovic 1996; Werner 1997; Pohanka 1998; Holstein et al. 1999; Smith 2000; Scheeres et al. 2000; Nagy et al. 2000; Garcia-Abdeslem and Martin-Atienza 2001; Tsoulis and Petrovic 2001; Smith et al. 2001; Singh and Guptasarma 2001; Holstein 2002, 2003; Korycansky 2004; Garcia-Abdeslem 2005; Werner and Scheeres 2005; Fahnestock and Scheeres 2006; Hamayun et al. 2009; Tsoulis et al. 2009;

Finite Body and its Brillouin Sphere

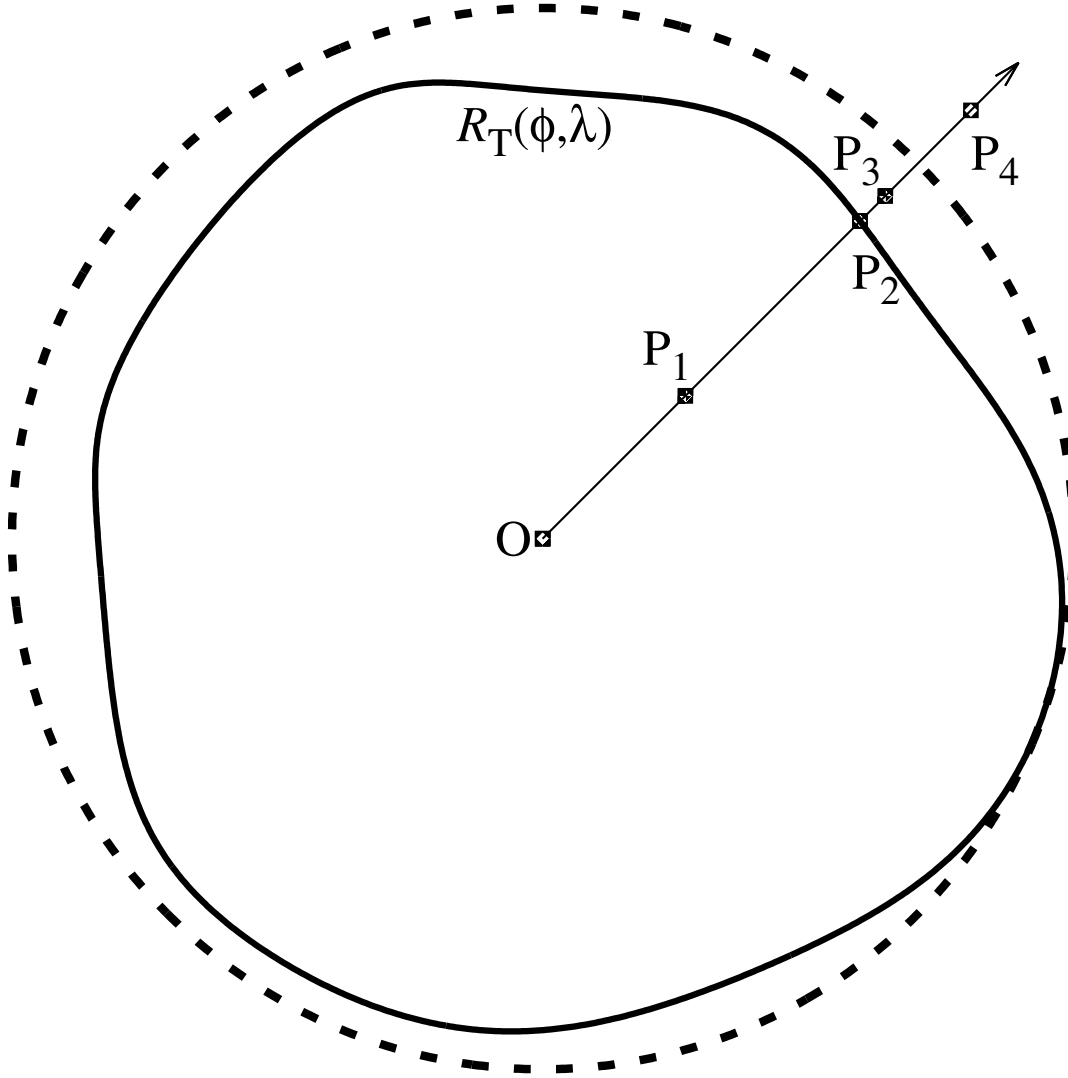


Figure 1. Sketch of Brillouin sphere. Shown is a meridional cross section of a finite body expressed by a solid curve, $R_T(\phi, \lambda)$, and its Brillouin sphere, namely the minimum concentric sphere including the body, indicated by a broken curve. Filled squares denote the origin, O , a point inside the body, P_1 , a point on the surface of the body, P_2 , a point outside the body but inside its Brillouin sphere, P_3 , and a point outside the Brillouin sphere, P_4 .

Tsoulis 2012; Takahashi et al. 2013; D’Urso 2013, 2014b; D’Urso and Trotta 2015; Chanut et al. 2015a; Zhao et al. 2016).

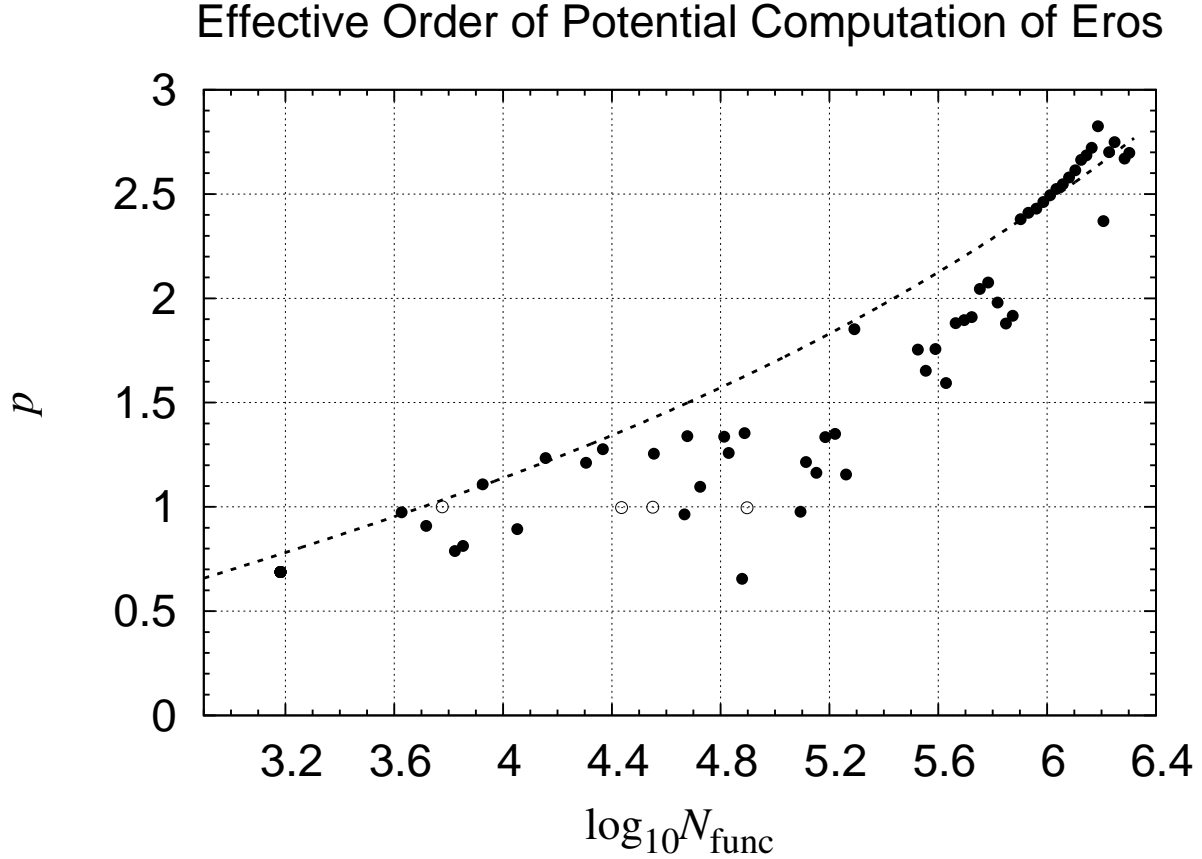


Figure 2. Effective order of gravitational potential computation. Shown are $p \equiv [\log_{10}(\delta V_0/\delta V)] / (\log_{10} N_{\text{func}})$, the effective order of computing the gravitational potential of the asteroid Eros at its coordinate center. Compared are the polyhedron models (D’Urso 2014a) marked by open circles and the new method indicated by filled circles. Here δV is the relative error measured as the difference with the reference solution obtained by the quadruple precision integration with a tiny value of the input relative error tolerance, N_{func} is the number of transcendental function evaluations such as the logarithm, trigonometric, and inverse trigonometric functions, and $\delta V_0 = 0.015$ is a numerical constant so that the results of the polyhedron model reproduce the theoretical value of the effective order, $p = 1$. The effective orders of the new method are not constant but increase exponentially with respect to N_{func} . The broken line shows its model curve expressed as $p_{\text{model}} = [\exp(0.47 \log_{10} N_{\text{func}}) - 2.0] / (\log_{10} N_{\text{func}})$.

Nevertheless, the polyhedron model is only an approximation. Indeed, its approximation error is non negligible even if the polyhedron field itself is precisely computed

(Conway 2015). For example, an analysis of the computed values of the gravitational potential of Eros at its coordinate center for the four polyhedron models with different number of faces: $N_{\text{face}} = 1708, 7790, 10152$, and 22540 (D’Urso 2014a), revealed that the computational error is inversely proportional to N_{face} . Since the computational labor is in proportion to N_{face} , the polyhedron model is an approximation method of the order 1 as

$$\delta V = \delta V_0 (N_{\text{func}})^{-1}, \quad (3)$$

where δV is the relative error measured as the difference with the reference solution, N_{func} is the number of transcendental function evaluations required in the potential computation such as the logarithm and inverse trigonometric functions, and $\delta V_0 = 0.015$ is a numerical constant. Refer to Fig. 2 illustrating the effective order defined as

$$p \equiv \frac{\log_{10}(\delta V_0/\delta V)}{\log_{10} N_{\text{func}}}. \quad (4)$$

In the figure, the open circles show the results of the polyhedron models. The constant value of p indicates that the relative error decreases in proportion to $(N_{\text{func}})^{-p}$ where N_{func} is obtained from N_{face} as $N_{\text{func}} = 3.5N_{\text{face}}$ in the computational procedure of the polyhedron models (D’Urso 2014a).

In any case, the observed order of the polyhedron models is too low to obtain precise gravitational fields efficiently. This is the reason why, in geodesy, intensively investigated is not the polyhedron models but the high order numerical quadrature of the tesseroïd¹ models despite that no analytical solution is known for the gravitational field of a tesseroïd and its spheroidal extension, and therefore the computational cost of its numerical integration is large (Huang et al. 2001; Novak and Grafarend 2005; Asgharzadeh et al. 2007; Han and Shen 2010; Tsoulis 2012; Tsoulis et al. 2012; Grombein et al. 2013; Hirt and Kuhn 2014; Roussel et al. 2015; Du et al. 2015; Wu 2016; Shen and Deng 2016).

Recently, we have completely resolved the problem of the algebraic singularities in $V(\mathbf{X})$ and $\mathbf{a}(\mathbf{X})$ (Fukushima 2016e). The key of success is the regularization of the Newton kernels, $1/|\mathbf{x} - \mathbf{X}|$ and/or $1/|\mathbf{x} - \mathbf{X}|^2$, by the integral variable transformation using the spherical polar coordinates centered at the evaluation point. The rewritten forms of $V(\mathbf{X})$ and $\mathbf{a}(\mathbf{X})$ can be properly integrated for any form of $\rho(\mathbf{x})$ by the standard numerical quadrature methods (Press et al. 2007, Chapt. 4). Having said that, we must confess that the computational burden to integrate them is huge (Fukushima 2016e, Figs 15 and 16). This is because the regularized integrals remain to be three-dimensional.

In the case of the solar system objects, $\rho(\mathbf{x})$ is piecewise constant or well approximated by a low degree polynomial in the radial direction. This fact enables us to reduce the dimension of the potential integration from three to two as will be seen

¹ A tesseroïd is a finite volume enclosed by two meridians, two parallels, and two spherical surfaces (Anderson 1976). It is sometimes called a spherical prism.

later. After the reduction, nevertheless, the integrand of the two-dimensional integral of the gravitational potential becomes logarithmically singular if the evaluation point is on the surface of or inside the object. Of course, the singularity is weak, and therefore, integrable in principle. However, their numerical integration had been difficult (Klees 1996).

We have conquered this difficulty (Fukushima 2016a,d) by the combination of the split quadrature method (Fukushima 2014b) using the double exponential (DE) rule (Takahashi and Mori 1973, 1974) for the potential integration and the numerical differentiation of the numerically integrated potential by Ridders' method (Ridders 1982) for the acceleration computation. Later we noticed that Ridders' method can be replaced by its simpler substitute: the central or single-sided difference formulas with an appropriate choice of the trial argument difference (Fukushima 2017). This replacement is in order to decrease the computational cost of the device.

Anyhow, by using the improved formulation, we succeeded to construct a precise and fast method of the gravitational field computation of a general finite body. Refer to Fig. 2 again. It compares the cost performance of the new method with that of the polyhedron model in evaluating the gravitational potential of Eros. Clearly, the new method is of the higher cost performance since its effective order is typically higher than that of the polyhedron model, especially when the high precision is required.

Below, we explain the new method in Sect. 2, and present its numerical experiments in Sect. 3. Also, we prepared the appendices containing the derivation of the formulas used in the new method, the description of the coefficient functions in the transformed integrand, a rewriting of the integrand to avoid the cancellation in its computation when the object consists of thin layers, a pair of Fortran subroutines to execute the double exponential quadrature in the double and quadruple precision environment, respectively, the results of some numerical experiments to confirm their good cost performance, and a Fortran function to compute a special logarithm function which is the key component of the integrand evaluated in the new method.

2. METHOD

2.1. *Surface integral expression of gravitational potential*

Let us consider the gravitational potential of a general finite body like solar system objects. It is mathematically described as a volume integral in Eq.(1). Without losing generality, we assume that the body is composed of multiple layers and all the layers are well defined in a certain spherical polar coordinate system associated with the object. If this assumption is not satisfied in a single spherical polar coordinate system such as in the case of the comet 67P Churyumov-Gerasimenko (Jorda et al. 2016), one may separate the finite body into some pieces so that the radial uniqueness condition is satisfied in each piece after taking different spherical polar coordinate systems with appropriate shift of the coordinate centers.

At any rate, we denote by $R_T(\phi, \lambda)$ and $R_B(\phi, \lambda)$ the radii of the top and the bottom surfaces of the layer, respectively. They are uniquely defined as functions of the latitude ϕ and the longitude λ . Also, we write the volume mass density of the layer as $\rho(r, \phi, \lambda)$ where r is the radius vector. Hereafter, we will focus on the gravitational field of a single layer. Within the layer, we assume that $\rho(r, \phi, \lambda)$ is properly expanded as a low degree polynomial of r as

$$\rho(r, \phi, \lambda) = \sum_{n=0}^N \rho_n(\phi, \lambda) \left(\frac{r}{R_0} \right)^n, \quad (5)$$

where R_0 is a certain reference value of the radius and N is a certain integer, say in the range 0 to 5. In fact, the density profile of the Earth is approximated by piecewise linear or cubic polynomials (Dziewonski and Anderson 1981; Kennett 1998; Ganguly et al. 2009). Also the density profile of the tropospheric air mass is representable by a quintic polynomial (Karcol 2011). **The separation of r^n from the full expression of the density profile, $\rho(r, \phi, \lambda)$, is a central trick of the new method. Indeed, as will be seen later, the kernel function can be analytically integrable even after the inclusion of r^n .**

In any case, the gravitational potential of the layer at an arbitrary point is written as a similar finite series as

$$V(R, \Phi, \Lambda) = \sum_{n=0}^N V_n(R, \Phi, \Lambda), \quad (6)$$

where (R, Φ, Λ) is the spherical polar coordinates of the evaluation point. Each term of the potential is expressed as a volume integral in the spherical polar coordinate system as

$$V_n(R, \Phi, \Lambda) \equiv \frac{G}{R_0} \int_{-\pi/2}^{\pi/2} \left[\int_0^{2\pi} \rho_n(\phi, \lambda) \left(\int_{R_B(\phi, \lambda)}^{R_T(\phi, \lambda)} \frac{r^2}{S(r, \phi, \lambda)} \left(\frac{r}{R_0} \right)^n dr \right) d\lambda \right] \cos \phi d\phi. \quad (7)$$

Here $S(r, \phi, \lambda)$ is a square root representing the normalized distance between the internal and evaluation points as

$$S(r, \phi, \lambda) \equiv \sqrt{A(\phi, \lambda) + [B(\phi, \lambda) + \zeta]^2}, \quad (8)$$

where $A(\phi, \lambda)$ and $B(\phi, \lambda)$ are a pair of auxiliary functions defined as

$$A(\phi, \lambda) \equiv B(\phi, \lambda) [2\alpha - B(\phi, \lambda)], \quad (9)$$

$$B(\phi, \lambda) \equiv 2\alpha \left[\sin^2 \left(\frac{\xi}{2} \right) + \cos \phi \cos \Phi \sin^2 \left(\frac{\eta}{2} \right) \right], \quad (10)$$

and α , ξ , η , and ζ are non dimensional quantities defined as

$$\alpha \equiv \frac{R}{R_0}, \quad \xi \equiv \phi - \Phi, \quad \eta \equiv \lambda - \Lambda, \quad \zeta \equiv \frac{r - R}{R_0}. \quad (11)$$

The innermost line integral of $V_n(R, \Phi, \Lambda)$, namely that with respect to r , can be analytically evaluated in a closed form as explained in Appendix A. As a result, $V_n(R, \Phi, \Lambda)$ is rewritten as a surface integral as

$$V_n(R, \Phi, \Lambda) = GR_0^2 \int_{-\pi/2}^{\pi/2} \left(\int_0^{2\pi} \rho_n(\phi, \lambda) K_n(\phi, \lambda) d\lambda \right) \cos \phi d\phi, \quad (12)$$

where $K_n(\phi, \lambda)$ is the kernel function of degree n defined as a difference of integrals as

$$K_n(\phi, \lambda) \equiv I_n(R_T(\phi, \lambda), \phi, \lambda) - I_n(R_B(\phi, \lambda), \phi, \lambda), \quad (13)$$

while $I_n(r, \phi, \lambda)$ is an indefinite line integral defined and analytically expressed as

$$I_n(r, \phi, \lambda) \equiv \frac{1}{R_0^{n+3}} \int^r \frac{(r')^{n+2} dr'}{S(r', \phi, \lambda)} = C_n(\phi, \lambda) L(r, \phi, \lambda) + D_n(r, \phi, \lambda) S(r, \phi, \lambda). \quad (14)$$

Here $L(r, \phi, \lambda)$ is a logarithmic function conditionally defined as

$$L(r, \phi, \lambda) \equiv \begin{cases} \ln [S(r, \phi, \lambda) + B(\phi, \lambda) + \zeta], & (B(\phi, \lambda) + \zeta \geq 0), \\ \ln [A(\phi, \lambda) / \{S(r, \phi, \lambda) - B(\phi, \lambda) - \zeta\}], & (B(\phi, \lambda) + \zeta < 0), \end{cases} \quad (15)$$

and $C_n(\phi, \lambda)$ and $D_n(r, \phi, \lambda)$ are the coefficient functions of degree n defined as polynomials of $B(\phi, \lambda)$, α , and ζ . The first **four pairs** are explicitly displayed here as

$$C_0 \equiv \alpha^2 - 3\alpha B + \frac{3}{2}B^2, \quad (16)$$

$$D_0 \equiv \left(2\alpha - \frac{3}{2}B \right) + \frac{1}{2}\zeta, \quad (17)$$

$$C_1 \equiv (\alpha - B) \left(\alpha^2 - 5\alpha B + \frac{5}{2}B^2 \right), \quad (18)$$

$$D_1 \equiv \left(3\alpha^2 - \frac{35}{6}\alpha B + \frac{5}{2}B^2 \right) + \left(\frac{3}{2}\alpha - \frac{5}{6}B \right) \zeta + \frac{1}{3}\zeta^2, \quad (19)$$

$$C_2 \equiv \alpha^4 - 10\alpha^3 B + \frac{45}{2}\alpha^2 B^2 - \frac{35}{2}\alpha B^3 + \frac{35}{8}B^4, \quad (20)$$

$$\begin{aligned} D_2 \equiv & \left(4\alpha^3 - \frac{43}{3}\alpha^2 B + \frac{175}{12}\alpha B^2 - \frac{35}{8}B^3 \right) + \left(3\alpha^2 - \frac{49}{12}\alpha B + \frac{35}{24}B^2 \right) \zeta \\ & + \left(\frac{4}{3}\alpha - \frac{7}{12}B \right) \zeta^2 + \frac{1}{4}\zeta^3, \end{aligned} \quad (21)$$

$$C_3 \equiv (\alpha - B) \left(\alpha^4 - 14\alpha^3 B + \frac{77}{2}\alpha^2 B^2 - \frac{63}{2}\alpha B^3 + \frac{63}{8}B^4 \right), \quad (22)$$

$$D_3 \equiv \left(5\alpha^4 - \frac{85}{3}\alpha^3 B + \frac{1001}{20}\alpha^2 B^2 - \frac{273}{8}\alpha B^3 + \frac{63}{8}B^4 \right)$$

$$\begin{aligned}
& + \left(5\alpha^3 - \frac{145}{12}\alpha^2 B + \frac{399}{40}\alpha B^2 - \frac{21}{8}B^3 \right) \zeta + \left(\frac{10}{3}\alpha^2 - \frac{69}{20}\alpha B + \frac{21}{20}B^2 \right) \zeta^2 \\
& + \left(\frac{5}{4}\alpha - \frac{9}{20}B^2 \right) \zeta^3 + \frac{1}{5}\zeta^4,
\end{aligned} \tag{23}$$

where we dropped the argument dependence for simplicity. Refer to Appendix A for a recursive algorithm to obtain the coefficient functions of arbitrary high degree. The correctness of the analytical expression of $I_n(r, \phi, \lambda)$, Eq. (14), is easily confirmed by its direct differentiation with respect to r .

Originally, the functions $S(r, \phi, \lambda)$, $A(\phi, \lambda)$, and $B(\phi, \lambda)$ are expressed as

$$S(r, \phi, \lambda) = \frac{\sqrt{R^2 - 2rR \cos \psi + r^2}}{R_0}, \tag{24}$$

$$A(\phi, \lambda) = \alpha^2 \sin^2 \psi, \tag{25}$$

$$B(\phi, \lambda) = 2\alpha \sin^2 \frac{\psi}{2}, \tag{26}$$

where ψ is the spherical angle between the direction vectors toward the internal and the evaluation points from the coordinate center such that

$$\cos \psi = \sin \phi \sin \Phi + \cos \phi \cos \Phi \cos(\lambda - \Lambda). \tag{27}$$

Nevertheless, the computation of ψ from this conventional definition suffers from a cancellation problem when $\phi \approx \Phi$ and $\lambda \approx \Lambda$, and therefore $\psi \approx 0$. This is the reason why we use the rewritten expressions of $A(\phi, \lambda)$ and $B(\phi, \lambda)$, equations (9) and (10), which are robust against the smallness of $\xi = \phi - \Phi$ and $\eta = \lambda - \Lambda$. Refer to Appendix A for a more detailed explanation.

Anyhow, the analytical expression of $I_n(r, \phi, \lambda)$, equation (14), is not found in the literature. Although the lowest degree expression, $I_0(r, \phi, \lambda)$, is mathematically equivalent with the existing form (Heck and Seitz 2007, equation (20)), the rewritten expression here is numerically more stable in the sense that no cancellation occurs when ξ and η are small, then $A(\phi, \lambda)$ and $B(\phi, \lambda)$ are also small, thus $S(r, \phi, \lambda) \approx |\zeta|$, and therefore $L(r, \phi, \lambda) \approx \ln(\zeta + |\zeta|)$ becomes large if $\zeta < 0$.

Notice that, if the layer is thin, the above expression of the kernel functions in a differenced form, equation (13), suffers from another kind of information loss. Refer to Appendix B for its cancellation-free rewriting. The robustness of the rewritten kernel functions is the key factor to ensure an accurate integration of the gravitational potential as will be seen later.

2.2. Split quadrature method using double exponential rule

Now, the problem is reduced to the evaluation of a weakly singular two-dimensional integral. Since the integral can not be analytically evaluated in a closed form, we evaluate it by a method of numerical quadrature.

When the evaluation point is inside or on the surface of the layer, the kernel functions, $K_n(\phi, \lambda)$, contain a logarithmically blowing-up singularity at the point of angular coincidence, namely when $\xi = \eta = 0$. This is because, in that case, the argument of the logarithm in $L(r, \phi, \lambda)$ reduces to the form of $\zeta + |\zeta|$, which can completely vanish if $\zeta \leq 0$. Also, even if the evaluation point is outside the layer such that $\zeta > 0$, the main functions, $L(r, \phi, \lambda)$ and $S(r, \phi, \lambda)$, have a sharp peak or a steep kink at the point of angular coincidence when $|\zeta|$ is sufficiently small. In such cases, the behavior of the integrand is difficult to be approximated as a low degree polynomial, which is the commonly assumed condition on which most of the ordinary quadrature rules are based. As a result, practical difficulties appear in the numerical integration by the standard numerical integrators like the Gauss-Legendre quadrature or the Romberg rule (Press et al. 2007, Chapt. 4).

In order to circumvent this difficulty, we adopt the double exponential (DE) rule (Takahashi and Mori 1973, 1974) as a method of the numerical integration. In short, the DE rule is the Romberg rule applied to the integrand transformed by the so-called TANH-SINH transformation and other integral variable transformations of double exponential nature (Press et al. 2007, Sect. 4.5). It is known as one of the best quadrature rules (Bailey et al. 2005). This is because the integration error typically decreases exponentially with respect to the number of integrand evaluations.

Also, the DE rule is easy to use since its algorithm is adaptive. In fact, one only has to specify δ , the input relative error tolerance. Then, the algorithm automatically takes care of test integrations in the Romberg rule so as to minimize the number of integrand evaluations while satisfying the error requirement. Experimentally, we learn that the algorithm is so reliable in the sense that the achieved relative errors are usually less than the input requirement *if* the length of the integration interval after the transformation is appropriately chosen. For the readers' convenience, we added Appendix C describing `dqde`, a Fortran subroutine of the DE rule in the double precision environment with an optimal setting of the integration interval.

The DE rule is known to be able to integrate weakly singular and/or nearly singular integrals properly *if* the singularities and/or the point of peaks are located at the endpoints of the integration interval (Mori 1985). In the present case, the singularities and/or the sharp peaks are located at the point of angular coincidence, namely when $\xi = \eta = 0$. Therefore, we first change the integration variables from ϕ and λ to ξ and η , respectively. Next, we split the integration interval of ξ into the positive and negative parts. In general, one must also split the integration interval of η similarly. However, we only have to shift the transformed integration interval as $[0, 2\pi)$ in terms of not λ but η . This is because the integrand is of 2π periodicity with respect to λ .

In any case, the final form of the split quadrature becomes

$$V_n(R, \Phi, \Lambda) = \int_{-\pi/2-\Phi}^0 P_n(\xi) d\xi + \int_0^{\pi/2-\Phi} P_n(\xi) d\xi, \quad (28)$$

where the new integrand $P_n(\xi)$ is a definite line integral defined as

$$P_n(\xi) \equiv \int_0^{2\pi} Q_n(\xi, \eta) d\eta, \quad (29)$$

while $Q_n(\xi, \eta)$ is an abbreviation expressed as

$$Q_n(\xi, \eta) \equiv GR_0^2 \rho_n(\Phi + \xi, \Lambda + \eta) K_n(\Phi + \xi, \Lambda + \eta). \quad (30)$$

Of course, if the object is homogeneous, then we can set $N = 0$ and simplify the integrand Q_0 as $Q_0(\xi, \eta) = GR_0^2 \rho_{00} K_0(\Phi + \xi, \Lambda + \eta)$ where ρ_{00} is the constant density value of the object. In any case, we evaluate all the line integrals in Eqs (28) and (29) by the DE rule.

2.3. Numerical differentiation

Let us move to the computation of the gravitational force. In this case, the situation is significantly different. Even after the radial integration is analytically conducted, the numerical integration of its surface integral form suffers from the algebraic singularities (Klees and Lehmann 1998). Therefore, we adopt another approach: the numerical partial differentiation of the numerically integrated potential (Fukushima 2016a,d, 2017). Namely, assuming the availability of $V(\mathbf{X})$ for arbitrary values of \mathbf{X} , we obtain $\mathbf{a}(\mathbf{X})$, and other quantities defined as the partial derivatives in general, by *numerically* evaluating their definitions as partial derivatives of $V(\mathbf{X})$.

As the method of numerical differentiation, we once utilized Ridders' method (Ridders 1982). Of course, this is a sure method. Nevertheless, it is also true that its computational cost is significantly larger, say a few tens times more, than that of the potential. Thus, in order to reduce the computational labor while keeping the accuracy as much as possible, we replace it with a conditional switch between the central difference formula and the single-sided difference formulas (Fukushima 2017). More specifically speaking, as long as the following test displacement of the evaluation point do not cross the surface of the layer, we approximate the gravitational acceleration components in the spherical polar coordinate system by the central difference formula as

$$a_R(R, \Phi, \Lambda) \approx [V(R + \Delta R, \Phi, \Lambda) - V(R - \Delta R, \Phi, \Lambda)] / (2\Delta R), \quad (31)$$

$$a_\Phi(R, \Phi, \Lambda) \approx [V(R, \Phi + \Delta\Phi, \Lambda) - V(R, \Phi - \Delta\Phi, \Lambda)] / (2R\Delta\Phi), \quad (32)$$

$$a_\Lambda(R, \Phi, \Lambda) \approx [V(R, \Phi, \Lambda + \Delta\Lambda) - V(R, \Phi, \Lambda - \Delta\Lambda)] / [2(R \cos \Phi) \Delta\Lambda], \quad (33)$$

by setting the test displacements in the spherical polar coordinates as

$$\Delta R/R = \Delta\Phi = \Delta\Lambda = \delta_2, \quad (34)$$

where we set the relative displacement as

$$\delta_2 = \sqrt[3]{\delta}. \quad (35)$$

This expression of the test displacement is obtained by equating the approximation error of the central difference formula with the input relative error of the potential integration (Press et al. 2007, Sect. 5.7) after approximating the behavior of the potential and its third order partial derivatives as those of a masspoint.

On the other hand, if any of the above test displacements crosses the surface of the layer, we compute the gravitational acceleration vector by appropriately chosen single-sided difference formulas such as

$$a_R(R, \Phi, \Lambda) \approx [V(R + \Delta R, \Phi, \Lambda) - V(R, \Phi, \Lambda)] / (\Delta R), \quad (36)$$

$$a_\Phi(R, \Phi, \Lambda) \approx [V(R, \Phi + \Delta \Phi, \Lambda) - V(R, \Phi, \Lambda)] / (R \Delta \Phi), \quad (37)$$

$$a_\Lambda(R, \Phi, \Lambda) \approx [V(R, \Phi, \Lambda + \Delta \Lambda) - V(R, \Phi, \Lambda)] / [(R \cos \Phi) \Delta \Lambda], \quad (38)$$

or

$$a_R(R, \Phi, \Lambda) \approx [V(R, \Phi, \Lambda) - V(R - \Delta R, \Phi, \Lambda)] / (\Delta R), \quad (39)$$

$$a_\Phi(R, \Phi, \Lambda) \approx [V(R, \Phi, \Lambda) - V(R, \Phi - \Delta \Phi, \Lambda)] / (R \Delta \Phi), \quad (40)$$

$$a_\Lambda(R, \Phi, \Lambda) \approx [V(R, \Phi, \Lambda) - V(R, \Phi, \Lambda - \Delta \Lambda)] / [(R \cos \Phi) \Delta \Lambda]. \quad (41)$$

This time, we set the test displacements in the spherical polar coordinates as

$$\Delta R / R = \Delta \Phi = \Delta \Lambda = \delta_1, \quad (42)$$

where a new relative displacement is chosen as

$$\delta_1 = \sqrt{\delta}. \quad (43)$$

It is determined by equating the approximation error of the single-sided difference formulas with the input relative error of the potential integration (Press et al. 2007, Sect. 5.7) after approximating the behavior of the potential and its second order partial derivatives as those of a masspoint. Of course, the input relative error tolerance of the potential integration, δ , is different from the achieved accuracy of the potential integrated. However, as will be shown later, we confirm that δ is a reliable indicator of the actual integration error. Therefore, we used the former as an appropriate estimate of the latter.

Anyhow, the expected relative accuracy of thus approximated gravitational acceleration vector is $\delta_2^2 = \sqrt[3]{\delta^2}$ for the central difference formulas and $\delta_1 = \sqrt{\delta}$ for the single-sided difference formulas, respectively. For example, if we set $\delta = 10^{-12}$, then $\delta_2 = 10^{-4}$ and $\delta_1 = 10^{-6}$, and therefore, we may anticipate the 8 digit accuracy of the gravitational acceleration components if the evaluation point is far from the surface and the 6 digit accuracy if near the surface.

The computational cost for each component of the acceleration vector is twice as much as that of the gravitational potential if the central difference formula is employed. Thus, the total CPU time to obtain the full acceleration vector becomes 6

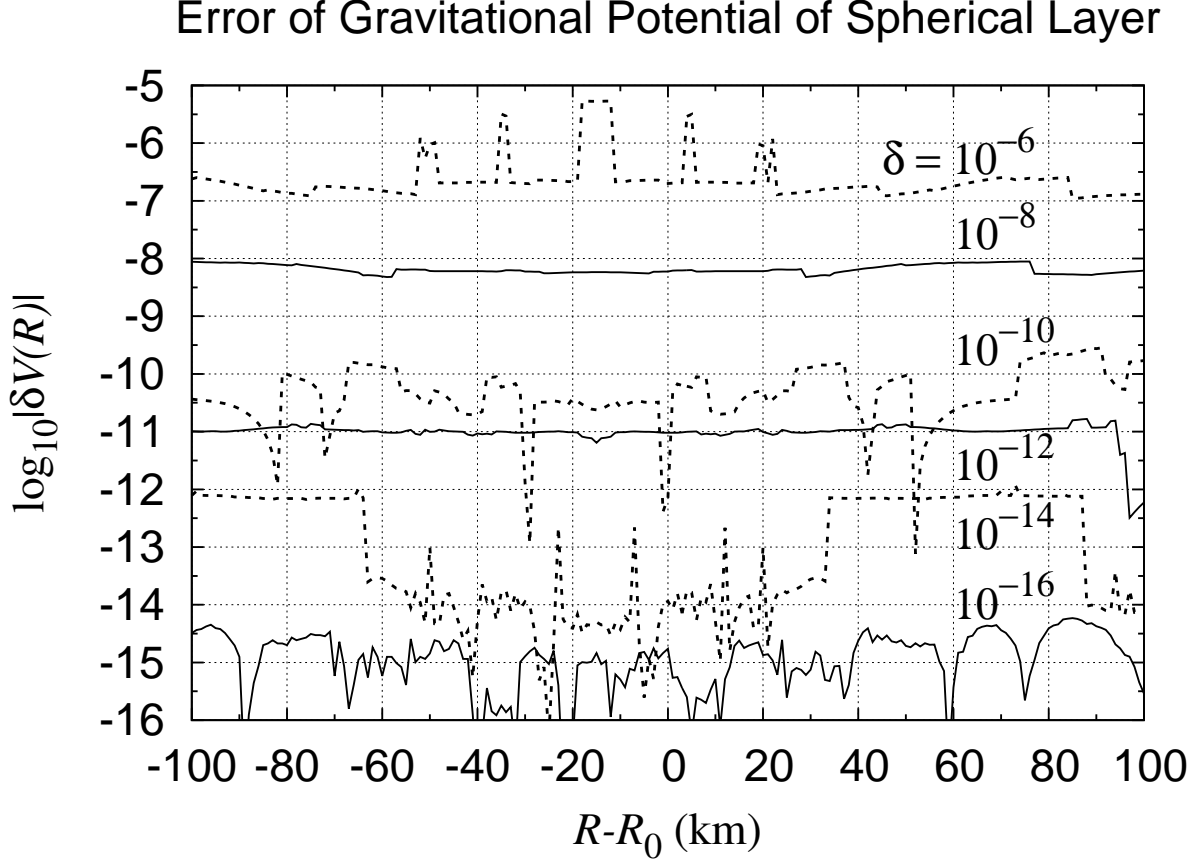


Figure 3. Relative error of gravitational potential of spherical layer. Plotted are the base-10 logarithm of the magnitude of the relative errors of the gravitational potential, $\delta V \equiv V_{\text{integrated}}/V_{\text{exact}} - 1$. Shown are the results for some values of δ , the input relative error tolerance for the DE quadrature rule as $\delta = 10^{-6}$, 10^{-8} , 10^{-10} , 10^{-12} , 10^{-14} , and 10^{-16} in the double precision environment.

times larger. On the other hand, if the single-sided difference formula is used, the extra computational cost per component is the same as that of the potential. Since the base potential value can be shared, the total computational labor is only 4 times larger.

3. NUMERICAL EXPERIMENTS

3.1. *Homogeneous Spherical Layer*

Below, we shall show the computational performance of the new method. Let us begin with the case where the analytical solution is known: a homogeneous spherical layer. We denote the reference radius and the top and bottom surface radii of the

layer by R_0 , R_T , and R_B , respectively. Then, the gravitational potential of the layer at a given radius R is expressed as

$$V(R) \equiv \begin{cases} 2\pi G\rho(R_T + R_B)H, & (0 \leq R < R_B), \\ (2\pi G\rho/3)(3R_T^2 - R^2 - 2R_B^3/R), & (R_B \leq R < R_T), \\ GM/R, & (R_T \leq R), \end{cases} \quad (44)$$

where ρ is the constant density of the layer, $H \equiv R_T - R_B$ is the thickness of the layer, and M is the mass of the layer expressed as

$$M \equiv (4\pi/3)\rho(R_T^2 + R_T R_B + R_B^2)H. \quad (45)$$

The radial component of the gravitational force is expressed as

$$a(R) \equiv \frac{dV(R)}{dR} = \begin{cases} 0, & (0 \leq R < R_B), \\ (4\pi G\rho/3)(-R + R_B^3/R^2), & (R_B \leq R < R_T), \\ -GM/R^2, & (R_T \leq R). \end{cases} \quad (46)$$

As a test case, we set $R_0 = 6380$ km, $R_T = R_0 + 10$ km, and $R_B = R_0 - 40$ km so as to model a spherical crust of the Earth. Then, we measured the relative errors of the gravitational potential integrated by the new method by comparing with the exact solution as

$$\delta V \equiv (V_{\text{integrated}} - V_{\text{exact}})/V_{\text{exact}}. \quad (47)$$

Figure 3 illustrates the measured errors as functions of R for various values of δ , the input relative error tolerance, in a logarithmic manner. The obtained errors are almost constant with respect to R , namely being independent on the location of the evaluation point. The relative errors of the integrated potential is roughly the same as δ if $\delta > 10^{-10}$. Otherwise, the errors increase by a factor 30 or so.

Let us move to the error of the computed acceleration vector. This time, the relative errors are not well defined since the exact value vanishes when $R < R_B$. Instead, we introduce the normalized error of acceleration defined as

$$\delta a \equiv (a_{\text{integrated}} - a_{\text{exact}})/a_{\text{max}}, \quad (48)$$

where $a_{\text{max}} \equiv a(R_T)$ is the maximum value of $a(R)$. Figure 4 depicts the normalized errors of the gravitational acceleration computed by the new method as functions of R . This time, they are mostly unchanged *if* outside the layer. In fact, the measured errors are roughly equal to $\sqrt[3]{\delta^2}$ as we expected. Inside the layer, however, the errors increase roughly by a factor 10–30. Also, the errors become large near the surface, say 6×10^{-5} when $\delta = 10^{-12}$.

Anyhow, if we add the contribution of the main part of the Earth, namely that of its mantle and cores, the relative magnitude of the computational errors of the

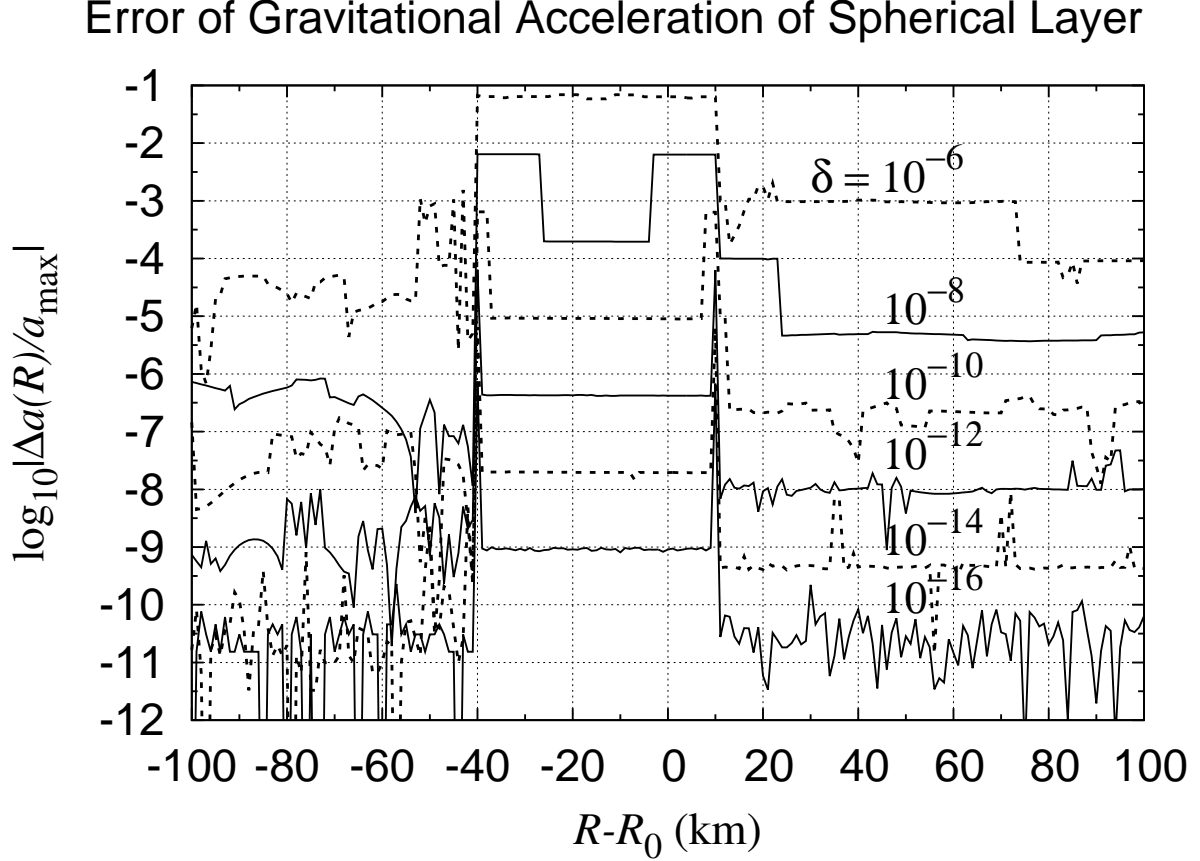


Figure 4. Normalized error of gravitational acceleration of spherical layer. Same as Fig. 3 but for the normalized errors of $a \equiv |\mathbf{a}|$, the magnitude of the gravitational acceleration vector, defined as $\delta a \equiv (a_{\text{integrated}} - a_{\text{exact}})/a_{\text{max}}$. Here a_{max} is the maximum value of the acceleration, namely that at $R = R_T$.

crustal component become much smaller, say by the factor of 10^{-3} – 10^{-4} . Therefore, we think that the new method can be sufficiently accurate in the computation of the gravitational field. This is so if the considered body is nearly spherical in the sense that the contribution of the non spherical part is relatively small such as the cases of Ceres, Vesta, Deimos, Phobos, and especially the asteroid Ryugu, the target object of HAYABUSA2 mission (Müller et al. 2017).

Finally, we measure the computational labor of the new method. Fig. 5 depicts N_{func} , the number of transcendental function evaluations required in computing the gravitational potential of the spherical layer by the new method. The figure illustrates the R -dependence of N_{func} . We omit the similar graphs showing the Φ - and Λ -dependences, respectively, since the results are practically the same as depicted in

Integration Cost of Gravitational Potential of Spherical Layer

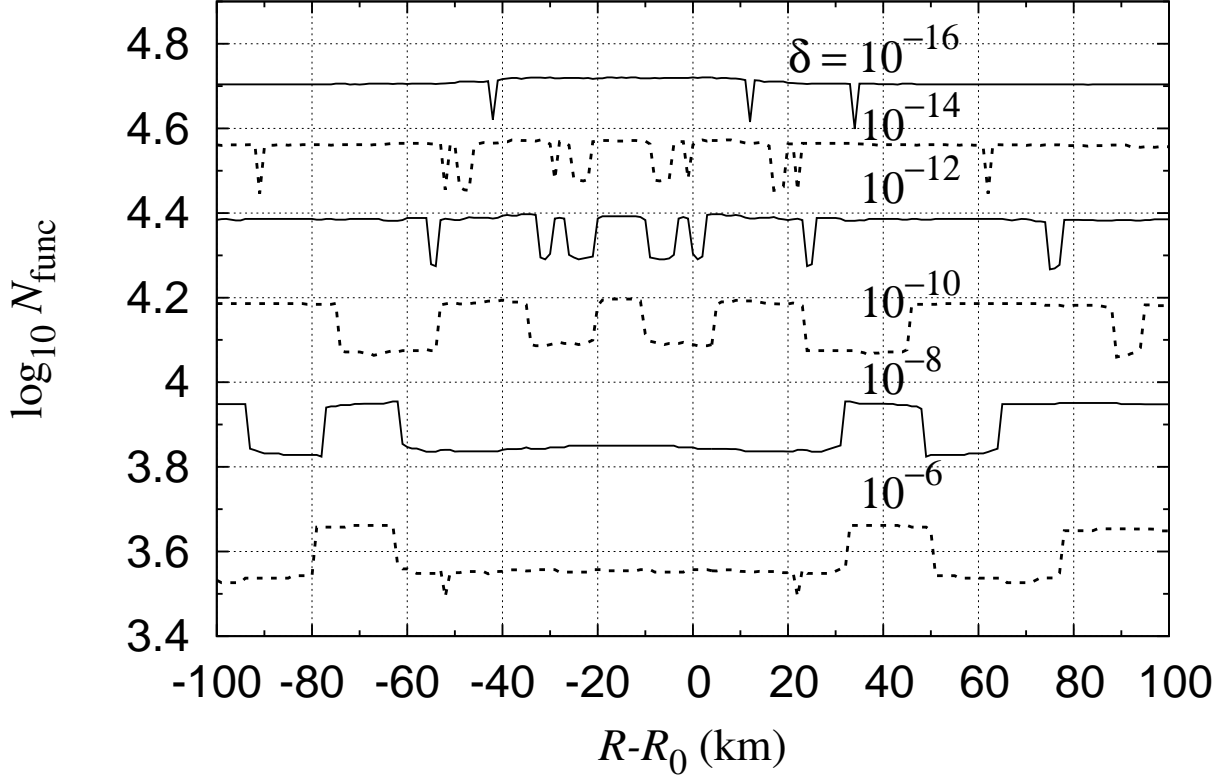


Figure 5. Integration cost of gravitational potential of spherical layer. Same as Fig. 3 but plotted are the base-10 logarithm of N_{func} , which is directly in proportion to the total CPU time. Obviously, the computational labor is almost independent on the location of the evaluation point. Sometimes, the total number is changed by a factor of 1.5 which corresponds to a constant step in the graph amounting $\log_{10} 1.5 \approx 0.176$. This incremental factor 1.5 corresponds to the doubling of the number of evaluation for one part of the split integral evaluation, which is caused because the DE rule is based on the Romberg quadrature method which automatically increases the number of integrand evaluation points in its test integrations by the mid-point rule.

Fig. 5. At this scale, the computational cost seems to be independent on the location of the evaluation point. This situation is the same as the polyhedron model. However, as will be seen later, the computational cost in actual cases reduces when the distance from the object increases significantly.

3.2. Asteroid Eros

As a more realistic example, let us investigate the gravitational field of 433 Eros. This is one of the most difficult cases of the gravitational field computation because the

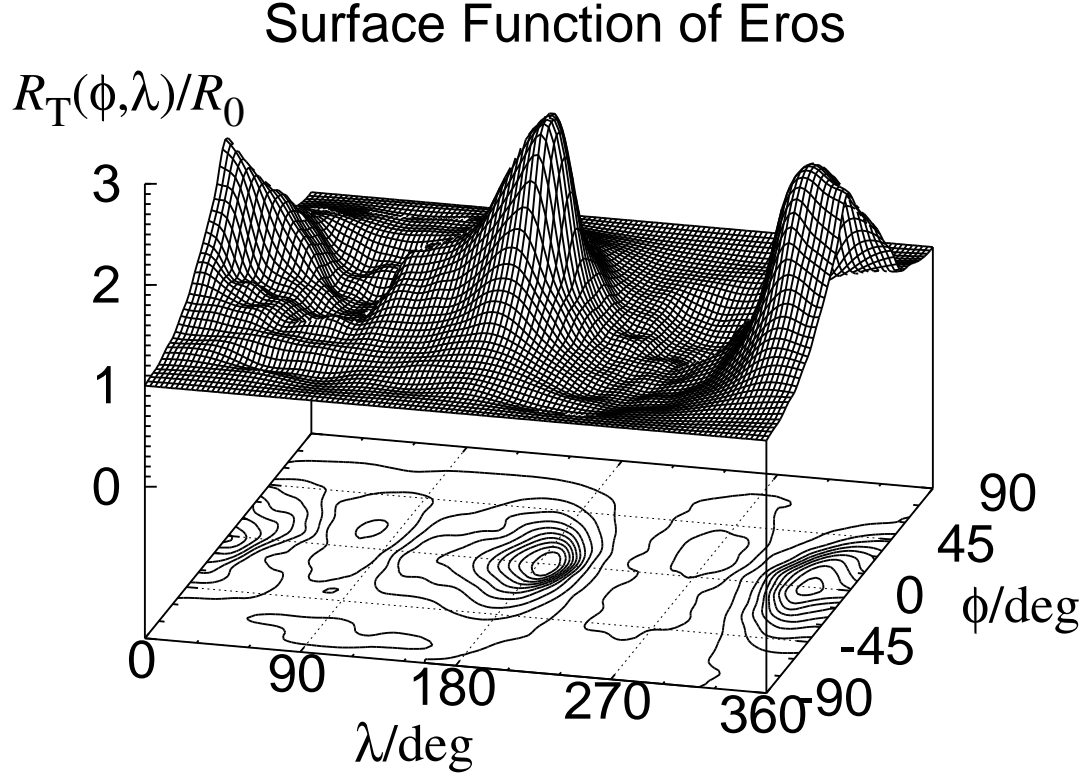


Figure 6. Surface function of Eros. Shown are a bird’s eye view and the associated contour map of the surface function of the asteroid Eros. Displayed is its shape modelled by a 24×24 spherical harmonic expansion (Miller et al. 2002) after normalization with $R_0 = 5.99276$ km, the reference radius defined as that at the north pole, $\phi = +90^\circ$. Two high mountains are actually the two edges of the elongated shape of the Eros. The maximum and minimum normalized radii are 2.9439 and 0.4902 achieved at $(\phi, \lambda) = (-4^\circ 10', 186^\circ 55')$ and $(+13^\circ 02', 273^\circ 27')$, respectively.

shape of the asteroid is significantly irregular. As its surface function, $R_T(\phi, \lambda)$, we used the 24×24 spherical harmonic expansion (Miller et al. 2002). Its bird’s eye view as well as the associated contour map are shown in Fig. 6. By setting $R_B(\phi, \lambda) = 0$ for simplicity and assuming the homogeneity of the asteroid, we integrated the grav-

itational potential, $V(R, \Phi, \Lambda)$, by setting $\delta = 10^{-12}$, and computed the acceleration vector, $\mathbf{a}(R, \Phi, \Lambda)$, by setting $\delta_2 = 10^{-4}$ far from the surface and $\delta_1 = 10^{-6}$ near the surface.

Figs 7 and 8 depict a bird's eye view and the associated contour map of the integrated potential and the magnitude of the computed acceleration vector at a constant radius, respectively. They are drawn as two-dimensional map with respect to the angular coordinates. The chosen radius, $R = 2R_0$, represents a case of the intermediate zone, namely inside the Brillouin sphere but above the bottom of the surface of the object.

The displayed view/map of the potential are much smoother than those of the surface function, Fig. 6. This is due to the averaging nature of the gravitational field computation as we had experienced with that of the spiral galaxy M74 (Fukushima 2016b). On the other hand, those of the acceleration magnitude have a sharp kink on two oval-shaped loci. They roughly correspond to the cross section of the surface of Eros cut by the sphere of constant radius, $R = 2R_0$. This is natural because the density is discontinuous across the loci: finite inside the loci and zero outside them.

In order to show the non analyticity of the gravitational field more clearly, we prepared Figs 9 and 10 displaying the contour map of the gravitational potential and the magnitude of the gravitational acceleration evaluated on the equator, namely when $\Phi = 0$, respectively. The contours of the potential value become dense near the surface of the object. This implicitly shows the non analyticity there. The situation is similar to that of the potential map of some finite axisymmetric bodies (Fukushima 2016d, Appendices A and C). Also, the contours of the acceleration magnitude exhibit a sharp boundary, which is exactly coincides with the surface of the object. This is the same feature we experienced with that of the spherical layer in the previous subsection.

With an aim to clarify the non analytic feature of the gravitational field, we examined the radial variation of the gravitational field more closely. Refer to Fig. 11 plotting the potential and the three acceleration components along the direction passing through the lowest point of the surface of Eros. Again, we confirm that the acceleration components are continuous but not differentiable at the surface. This is because the potential curves are not analytic there.

We noticed that, even outside the object, all the acceleration components are not monotonically decreasing when R **increases**. The phenomenon is prominent near the surface, say when $0.5 < R/R_0 < 0.7$. Indeed, their peak values are achieved there. This interesting feature is caused by the gravitational attraction of mountainous area surrounding the lowest point.

On the other hand, Fig. 12 illustrates the radial variation of the computational cost of the gravitational potential. When the distance from the asteroid is large, the potential value is almost inversely proportional to R , the radial coordinate. Therefore, for an efficient computation, one may increase the relative error tolerance so as to be in

Gravitational Potential of Eros: $R=2R_0$

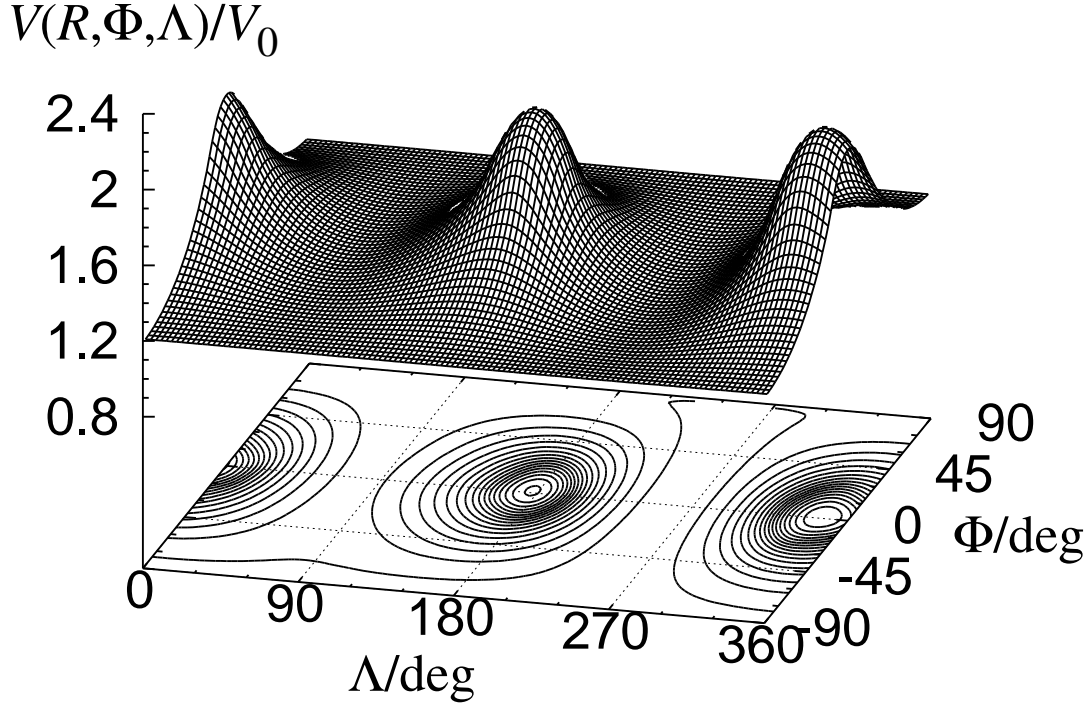


Figure 7. Gravitational potential of Eros on a spherical surface, $R = 2R_0$. Same as Fig 6 but for the gravitational potential of Eros on the spherical surface of a constant radius. Displayed is the result when $R = 2R_0$. The corresponding spherical surface is inside the Brillouin sphere but outside the bottom of the surface of Eros. The potential values are obtained by the new method with a sufficiently small relative error tolerance, $\delta = 10^{-12}$. The normalization constant of the potential is $V_0 \equiv (4\pi/3)G\rho R_0^2$, the surface potential value of a sphere of the radius R_0 with the same density. The curved surface of the potential mostly follow the bipolar feature of the surface function. However, the variation of the potential value is much smoother than that of the surface radius. This is due to the global nature of the gravitational field. A careful examination will reveal the non analyticity of the obtained curved surface of the potential value at the loci where $R = R_T(\phi, \lambda)$. Nevertheless, it is hardly visible at this scale.

Gravitational Acceleration of Eros: $R=2R_0$

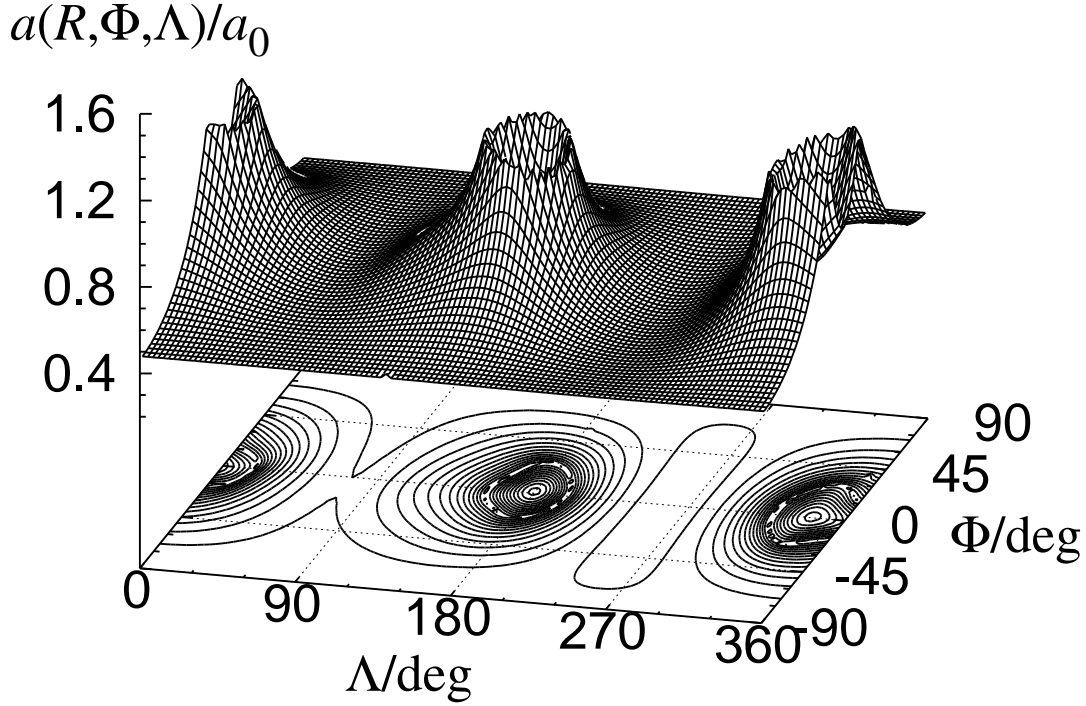


Figure 8. Gravitational acceleration of Eros on a spherical surface, $R = 2R_0$. Same as Fig 7 but for the magnitude of the gravitational acceleration vector, $a(R, \Phi, \Lambda) \equiv |\mathbf{a}(R, \Phi, \Lambda)|$. This time, the normalization constant is defined as $a_0 \equiv (4\pi/3)G\rho R_0$, namely the surface acceleration of a sphere of the radius R_0 with the same density. The acceleration magnitude becomes locally maximum at two oval shaped curves. They roughly represent the cross sections of the surface of the asteroid cut by the sphere of radius, $R = 2R_0$.

proportion to R . This policy decreases the computational cost as seen in Fig. 12. This feature is different from the polyhedron model which requires the same computational cost independently on the location of the evaluation point. Having said so, we must say that the spherical or spheroidal harmonic expansions are much more efficient *if outside* the Brillouin sphere or spheroid.

Cross Section of Eros Potential on Equator

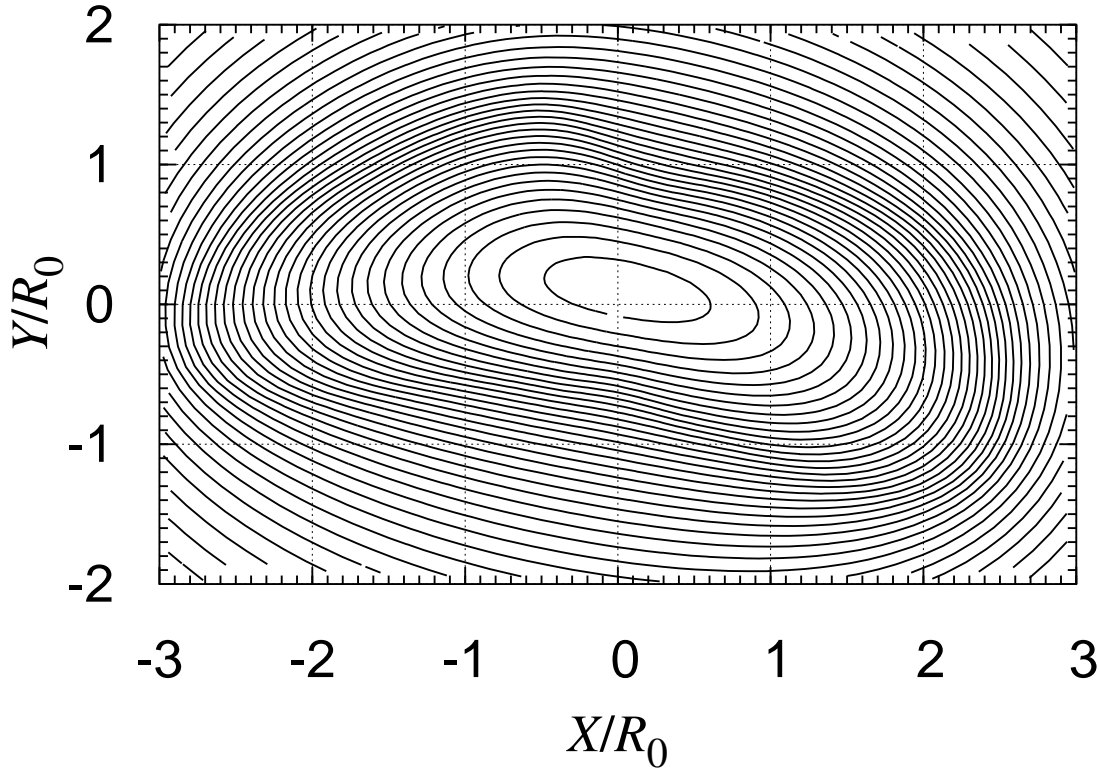


Figure 9. Equatorial cross section of gravitational potential of Eros. Depicted is the contour map of $V(R, 0, \Lambda)$, the gravitational potential of Eros on its equatorial cross section, namely when $\Phi = 0$. The X and Y coordinates are defined as $X \equiv R \cos \Lambda$ and $Y \equiv R \sin \Lambda$.

Let us focus on the gravitational feature on the surface, which is most difficult to obtain by the existing methods including the polyhedron models. Fig. 13 illustrates the bird's eye view and the associated contour map of the surface gravitational potential of the asteroid. By comparing it with Fig. 6, we notice that the magnitude of the surface potential is inversely correlated with the shape function. Namely, it becomes small in the mountainous area and large in the basins and valleys.

Next, we prepared Fig. 14 showing the similar view and map of the magnitude of the surface gravitational acceleration vector of the asteroid. This time, the variation of the magnitude of the acceleration vector is significantly smaller than those of the potential. Also, the magnitude of the acceleration is smaller not only in the mountainous area but also in the basins and valleys. Thirdly, we calculated the

Cross Section of Eros Acceleration on Equator

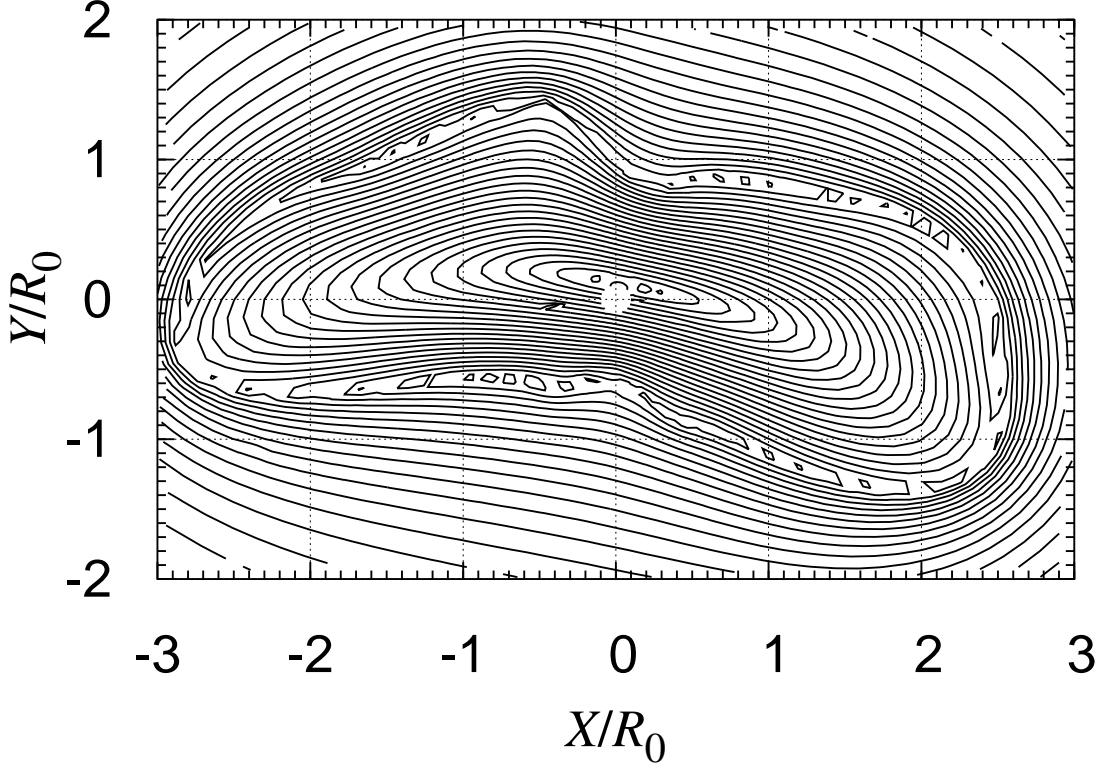


Figure 10. Equatorial cross section of magnitude of gravitational acceleration of Eros. Same as Fig. 9 but of $a(R, 0, \Lambda)$, the magnitude of the gravitational acceleration on the equator. The obtained values of a have a clear kink on the surface of the Eros. A careful comparison with Fig. 9 reveals that the contours observed here are not the same as those of the gravitational potential. This is because the contribution of the longitudinal component of the acceleration can not be retrievable from Fig. 9 only.

deflection angle of the surface acceleration vector,

$$\theta \equiv \tan^{-1} \left(\sqrt{a_{\Phi}^2 + a_{\Lambda}^2} / a_R \right). \quad (49)$$

Its bird's eye view and the associated contour map are provided in Fig. 15. The deflection angle is large in most areas, especially in the steep slopes of mountainous area. These facts will be important in designing the descending orbit of a space probe to land on irregular shaped objects (Liu et al. 2017).

4. CONCLUSION

Radial Variation of Potential and Acceleration of Eros

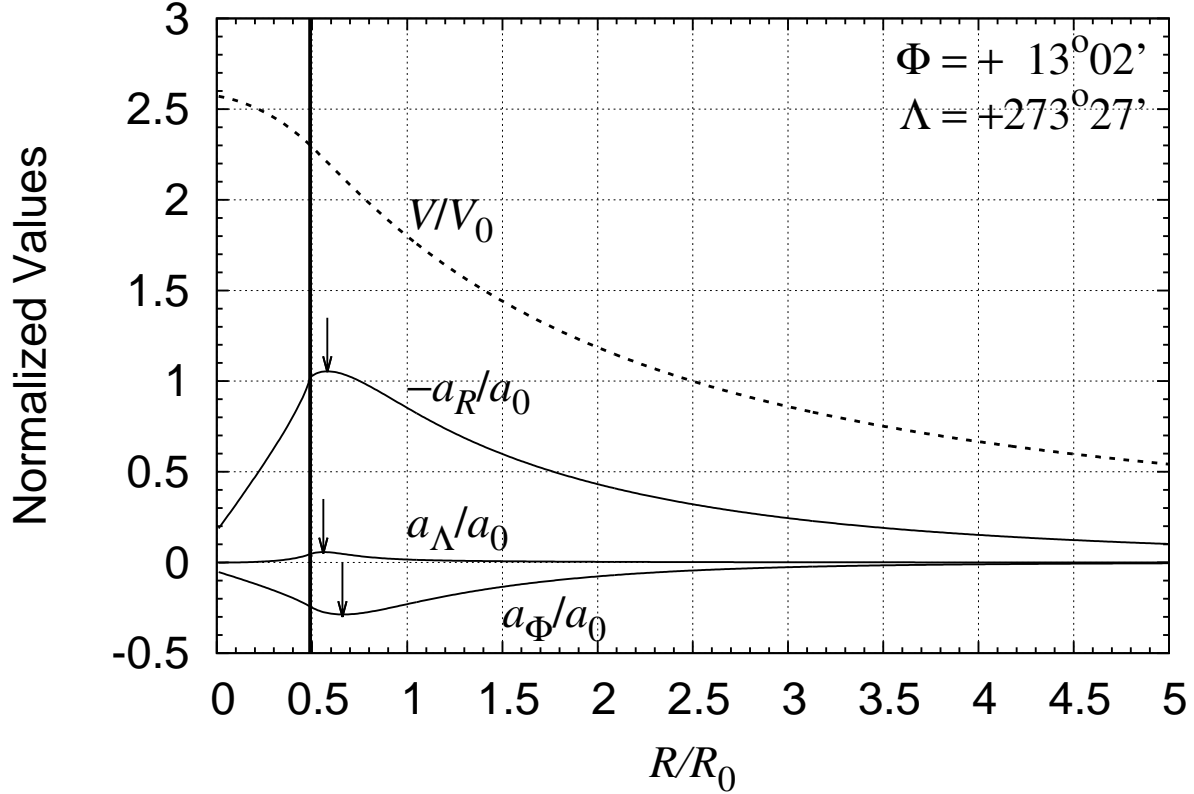


Figure 11. Radial variation of gravitational potential and acceleration vector. Plotted are the radial variation of the gravitational potential and three components of the gravitational acceleration vector of the Eros along the direction of the lowest point where $(\Phi, \Lambda) = (+13^{\circ}02', 273^{\circ}27')$. The vertical line is the location of the surface. Arrows indicate the peaks of gravitational acceleration components, which locate *outside* the surface.

In order to assist the orbit design of HAYABUSA2 and its probe MASCOT scheduled to land on 162173 Ryugu, we developed a new method to compute accurately the gravitational field of a general finite body. The new method consists of two parts: the numerical integration of the gravitational potential and the numerical differentiation of the numerically integrated potential to compute the gravitational acceleration. The integration method we adopted is the split quadrature using the double exponential rule. We applied this combination to the surface integral representation of the potential which was obtained by conducting the analytical integration of the radial part in a closed form. Meanwhile, we conditionally selected the central or the single-sided difference formulas in executing the numerical differentiation after setting the relative

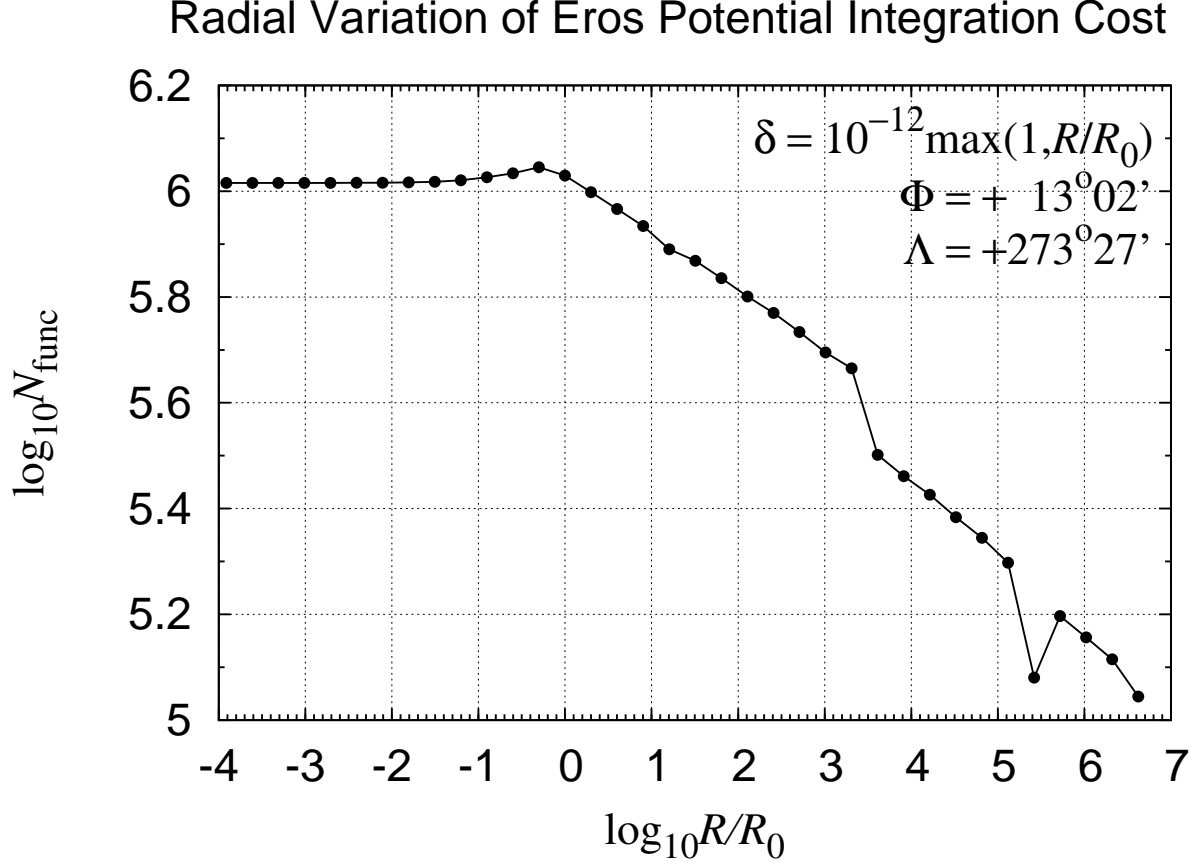


Figure 12. Radial variation of computational cost of Eros potential. Shown is the radial variation of the computational cost of the gravitational potential of the Eros along the direction of the lowest point where $(\Phi, \Lambda) = (+13^{\circ}02', 273^{\circ}27')$.

trial deviation of arguments as the cubic or square root of the relative error tolerance of the potential integration. The new method is capable to compute the gravitational field independently on the location of the evaluation point, namely whether inside, on the surface of, or outside the layer. Also, the method can be sufficiently accurate, say of 14–15 digits for the potential and of 9–10 digits for the acceleration vector, respectively. On the other hand, the computational efficiency of the new method is higher than that of the polyhedron models. This is mainly because the computational error of the new method decreases much faster than that of the polyhedron models when the computational labor is increased and partly because the integrand of the surface integral adopted in the new method calls only one transcendental function, a kind of special logarithm function, while the polyhedron models require one logarithm function for each edge and two arc tangent functions for each face to be computed.

Surface Gravitational Potential of Eros

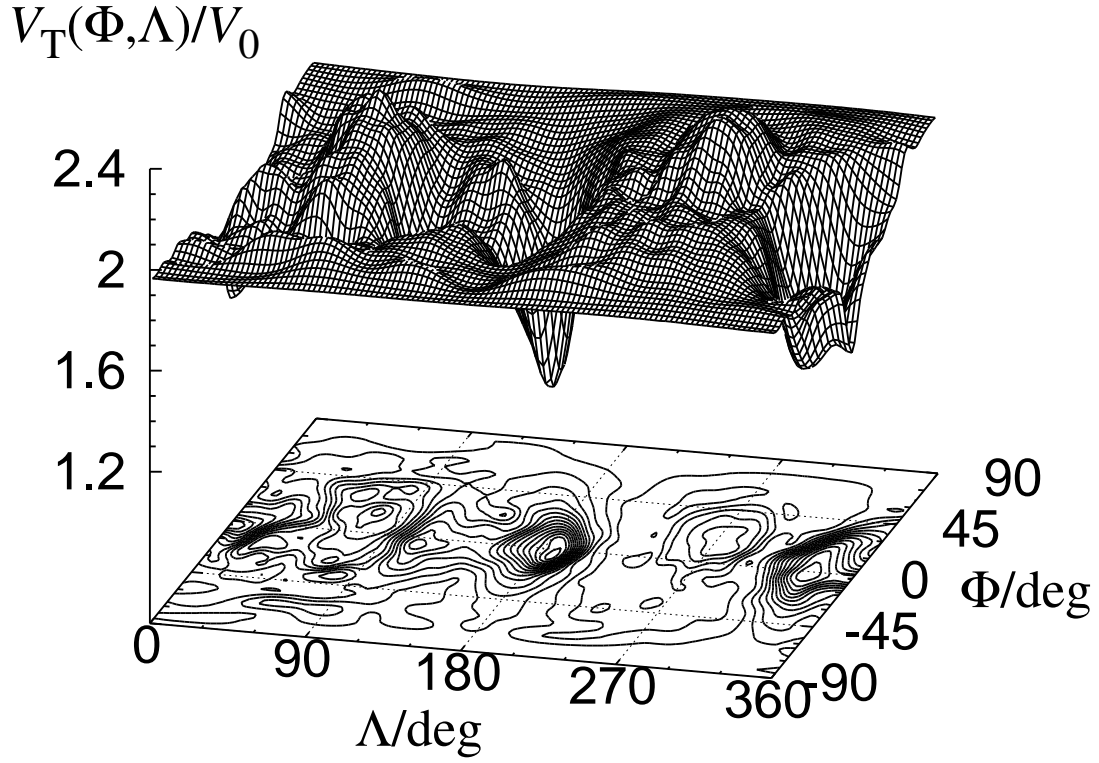


Figure 13. Surface gravitational potential of Eros. Same as Fig 7 but on the surface of Eros. Namely it displays $V_T(\Phi, \Lambda) \equiv V(R_T(\Phi, \Lambda), \Phi, \Lambda)$.

Surface Gravitational Acceleration of Eros

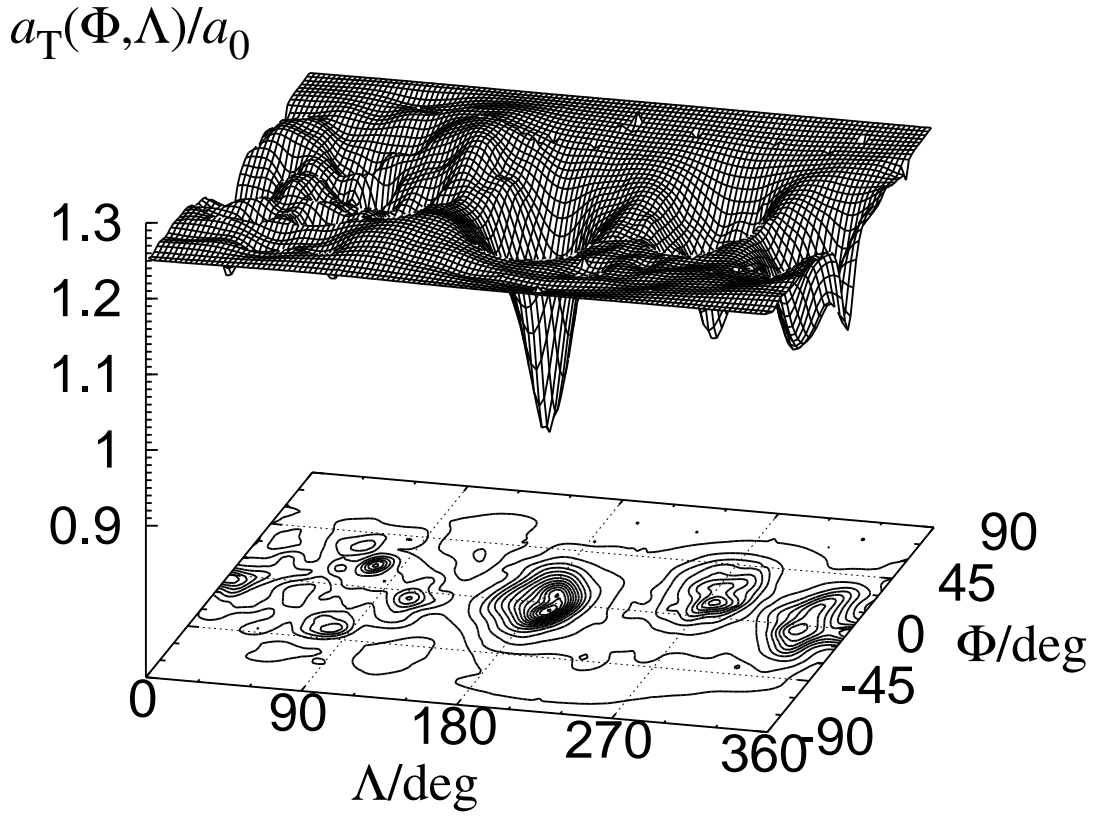


Figure 14. Magnitude of surface gravitational acceleration of Eros. Same as Fig. 13 but for the magnitude of the gravitational acceleration vector, $a_T(\Phi, \Lambda) \equiv |\mathbf{a}(R_T(\Phi, \Lambda), \Phi, \Lambda)|$.

Deflection of Surface Acceleration of Eros

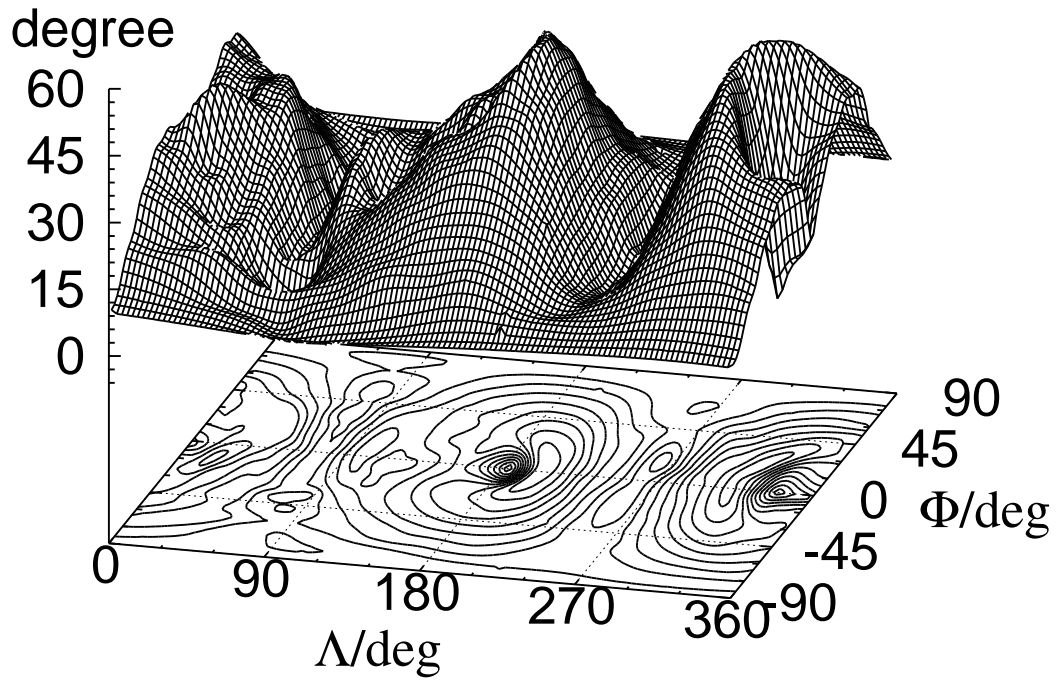


Figure 15. Deflection of surface gravitational acceleration vector of Eros. Same as Fig. 13 but for the magnitude of the deflection angle of the gravitational acceleration vector, $\theta \equiv \tan^{-1} \left(\sqrt{a_{\Phi}^2 + a_{\Lambda}^2} / a_R \right)$, on the surface of Eros.

The author appreciates the referee's valuable advices and comments to improve the quality and readability of the present article.

APPENDIX

A. DERIVATION OF ANALYTICAL EXPRESSION OF VERTICAL INTEGRALS

Let us derive the analytical expression of the innermost line integrals presented in the main text. For simplicity, we will omit the functional dependency on r , ϕ , and/or λ in this section.

A.1. *Mutual distance*

We begin with the expression of the **normalized** mutual distance, S . Using the spherical polar coordinates of the internal and evaluation points, \mathbf{x} expressed as (r, ϕ, λ) and \mathbf{X} expressed as (R, Φ, Λ) , we write the mutual distance as

$$|\mathbf{x} - \mathbf{X}| = \sqrt{r^2 - 2rR \cos \psi + R^2}, \quad (\text{A1})$$

where ψ is the angular distance between the direction vectors, \mathbf{x}/r and \mathbf{X}/R , such that its cosine is expressed as

$$\cos \psi = (\mathbf{x} \cdot \mathbf{X})/(rR) = \sin \phi \sin \Phi + \cos \phi \cos \Phi \cos(\lambda - \Lambda). \quad (\text{A2})$$

This expression is fragile against the proximity of \mathbf{x} and \mathbf{X} , namely when $\phi \approx \Phi$, $\lambda \approx \Lambda$, and/or $r \approx R$. In order to overcome the numerical problems caused by the proximity, we introduce new variables and an auxiliary quantity defined as

$$\xi \equiv \phi - \Phi, \quad \eta \equiv \lambda - \Lambda, \quad \zeta \equiv (r - R)/R_0, \quad \alpha \equiv R/R_0, \quad (\text{A3})$$

where R_0 is a certain scale constant. Using them, we first rewrite $\cos \psi$ as

$$\begin{aligned} \cos \psi &= \sin \phi \sin \Phi + \cos \phi \cos \Phi - \cos \phi \cos \Phi [1 - \cos(\lambda - \Lambda)] \\ &= \cos \xi - \cos \phi \cos \Phi (1 - \cos \eta). \end{aligned} \quad (\text{A4})$$

Next, we obtain a more robust form representing ψ as

$$\begin{aligned} \sin^2(\psi/2) &= (1 - \cos \psi)/2 = (1 - \cos \xi)/2 + \cos \phi \cos \Phi (1 - \cos \eta)/2 \\ &= \sin^2(\xi/2) + \cos \phi \cos \Phi \sin^2(\eta/2). \end{aligned} \quad (\text{A5})$$

After this preparation, we rewrite the normalized mutual distance, S , as

$$S \equiv |\mathbf{x} - \mathbf{X}|/R_0 = \sqrt{(r - R \cos \psi)^2 + R^2 \sin^2 \psi}/R_0 = \sqrt{(\zeta + B)^2 + A}, \quad (\text{A6})$$

where B and A are expressed as

$$\begin{aligned} B &= (R/R_0) (1 - \cos \psi) = 2\alpha \sin^2(\psi/2) \\ &= 2\alpha [\sin^2(\xi/2) + \cos \phi \cos \Phi \sin^2(\eta/2)], \end{aligned} \quad (\text{A7})$$

$$\begin{aligned} A &= (R/R_0)^2 \sin^2 \psi = \alpha^2 [2 \sin(\psi/2) \cos(\psi/2)]^2 \\ &= 2\alpha \sin^2(\psi/2) [2\alpha - 2\alpha \sin^2(\psi/2)] = B(2\alpha - B). \end{aligned} \quad (\text{A8})$$

Thus, we arrived at the expression of S in terms of A and B in the main text.

A.2. Radial integral

Next, we consider the radial integral I_n . It is compactly expressed as

$$\begin{aligned} I_n &= \frac{1}{R_0^{n+3}} \int^r \frac{(r')^{n+2} dr'}{S} = \int^\zeta \frac{(\zeta' + \alpha)^{n+2} d\zeta'}{\sqrt{(\zeta' + B)^2 + A}} = \int^{\zeta+B} \frac{(t + \alpha - B)^{n+2} dt}{\sqrt{t^2 + A}} \\ &= \sum_{j=0}^{n+2} \binom{n+2}{j} (\alpha - B)^{n+2-j} L_j(\zeta + B), \end{aligned} \quad (\text{A9})$$

where $L_j(t)$ is an indefinite integral defined as

$$L_j(t) \equiv \int^t \frac{\tau^j d\tau}{\sqrt{\tau^2 + A}}. \quad (\text{A10})$$

The integrand of $L_j(t)$ is of the form of a monomial of τ divided by a square root of a simple quadratic polynomial of τ . Thus, it can be analytically integrated in terms of elementary functions. For example, the first two of them are explicitly obtained as

$$L_0(t) = \ln \left(t + \sqrt{t^2 + A} \right) = L, \quad (\text{A11})$$

$$L_1(t) = \sqrt{t^2 + A} = S. \quad (\text{A12})$$

Namely they reduce to L and S introduced in the main text. For the computation of the higher order integrals, $L_j(t)$, we employ its recurrence relation as

$$jL_j(t) = t^{j-1}S - (j-1)AL_{j-2}, \quad (j = 2, 3, \dots), \quad (\text{A13})$$

by starting from a pair of initial values, $L_0(t)$ and $L_1(t)$. The correctness of the recurrence relation is easily confirmed by the direct differentiation. At any rate, $L_j(t)$ are mechanically obtained from the recurrence formula such as

$$2L_2 = tS - AL, \quad (\text{A14})$$

$$3L_3 = (t^2 - 2A)S, \quad (\text{A15})$$

where we omitted the dependency on t for further simplicity. Refer to [Karcol \(2011\)](#) presenting a slightly different derivation. In any case, it is trivial to see that these integration formulas result the expression of $C_j(\phi, \lambda)$ and $D_j(r, \phi, \lambda)$ for $j = 0, 1, 2, 3$ provided in the main text.

B. CANCELLATION-FREE REWRITING OF KERNEL FUNCTION

For simplicity, we will omit the angular dependence of quantities, namely that on ϕ and λ , in this section. The defining expression of the kernel function in the main text faces with a catastrophic cancellation for a thin layer, namely when $R_T \approx R_B$. In order to avoid the resulting unnecessary information loss, we rewrite the expression

in a cancellation-free form against the smallness of the **normalized** thickness of the boundary layer defined as

$$\beta \equiv \zeta_T - \zeta_B. \quad (\text{B16})$$

The rewritten expression of the kernel function is

$$K_n = J_n \cos \phi, \quad (\text{B17})$$

where J_n is a small quantity defined as

$$J_n \equiv C_n \log 1p \left[\left(\frac{1+T}{\zeta_B + B + S_B} \right) \beta \right] + [D_n(R_T) T + S_B E_n] \beta, \quad (\text{B18})$$

and T is a divided difference defined and explicitly expressed as

$$T \equiv \frac{S_T - S_B}{\beta} = \frac{\zeta_T + \zeta_B + 2B}{S_T + S_B}. \quad (\text{B19})$$

Here, S_T and S_B are the values of S on the surfaces of the object as

$$S_T \equiv S(R_T), \quad S_B \equiv S(R_B), \quad (\text{B20})$$

and E_n is an auxiliary function defined as a divided difference of $D_n(R)$ as

$$E_n \equiv [D_n(R_T) - D_n(R_B)] / \beta. \quad (\text{B21})$$

In the above, $\log 1p$ is a special logarithm function defined as

$$\log 1p(x) \equiv \ln(1+x) = x + \frac{x^2}{2} + \frac{x^3}{3} + \cdots, \quad (\text{B22})$$

which is efficiently computed by `dlog1p`, a Fortran 90 function listed in Table 2 of Appendix D. The cancellation-free expression of E_n for general index n is easily computable but complicated. Here, we explicitly provide some of them as

$$E_0 = \frac{1}{2}, \quad (\text{B23})$$

$$E_1 = \left(\frac{3}{2}\alpha - \frac{5}{6}B \right) + \frac{1}{3}(\zeta_T + \zeta_B), \quad (\text{B24})$$

$$E_2 = \left(3\alpha^2 - \frac{49}{12}\alpha B + \frac{35}{24}B^2 \right) + \left(\frac{4}{3}\alpha - \frac{7}{12}B \right) (\zeta_T + \zeta_B) + \frac{1}{4}(\zeta_T^2 + \zeta_T \zeta_B + \zeta_B^2), \quad (\text{B25})$$

$$E_3 = \left(5\alpha^3 - \frac{145}{12}\alpha^2 B + \frac{399}{40}\alpha B^2 - \frac{21}{8}B^3 \right) + \left(\frac{10}{3}\alpha^2 - \frac{69}{20}\alpha B + \frac{21}{20}B^2 \right) (\zeta_T + \zeta_B) + \left(\frac{5}{4}\alpha - \frac{9}{20}B^2 \right) (\zeta_T^2 + \zeta_T \zeta_B + \zeta_B^2) + \frac{1}{5}(\zeta_T^3 + \zeta_T^2 \zeta_B + \zeta_T \zeta_B^2 + \zeta_B^3). \quad (\text{B26})$$

C. FORTRAN PROGRAM OF DOUBLE EXPONENTIAL RULE

C.1. *Algorithm and implementation*

Here we provide a couple of Fortran programs to evaluate a line integral expressed as

$$s \equiv \int_a^b f(x)dx, \quad (\text{C27})$$

where $f(x)$ is either (i) regular in the whole integration interval, $a \leq x \leq b$, or (ii) regular inside the interval, $a < x < b$, and has integrable singularities or sharp peaks at one or multiple endpoints, namely when $x = a$ and/or $x = b$. As a basic method of its numerical evaluation, we adopt the double exponential rule using the TANH-SINH rule (Takahashi and Mori 1974).

The most problematic issue in its practical implementation is the truncation of the integration interval after the variable transformation, which is infinite by definition. More specifically speaking, we restrict the infinite interval, $(-\infty, +\infty)$, into a finite one, $(-h_{\max}, +h_{\max})$. Thus, the question is the choice of h_{\max} . If it is too small, the computational precision is degraded. Meanwhile, if it is too large, the computational labor becomes too much. Therefore, there is an optimal value of h_{\max} , which may depend on the general nature of the integrand before the transformation and the input relative error tolerance, δ .

After some preliminary experiments, we fixed its functional form of h_{\max} to be a piecewise polynomial of $\log_{10} \delta$ as

$$h_{\max} = p_j + q_j (-\log_{10} \delta), \quad (t_{j-1} < -\log_{10} \delta < t_j; \quad j = 1, 2, \dots, J), \quad (\text{C28})$$

where p_j , q_j , and t_j and the total number of pieces J are free parameters to be tuned. Then, by restricting the type of integrand to $\log(x-a)$ or $\log(b-x)$, we experimentally determined an optimal set of the parameters as

$$p_1 = 2.75, \quad q_1 = 0.75, \quad t_1 = 4, \quad (\text{C29})$$

$$p_2 = 3.75, \quad q_2 = 0.50, \quad t_2 = 6, \quad (\text{C30})$$

$$p_3 = 5.25, \quad q_3 = 0.25, \quad t_3 = 10, \quad (\text{C31})$$

$$p_4 = 6.50, \quad q_4 = 0.125, \quad t_4 = \infty, \quad (\text{C32})$$

while $t_0 = -\infty$.

Consequently, we implemented the algorithm into `dqde`, a Fortran subroutine in the double precision environment as listed in Table 1. Its quadruple precision extension, `qqde`, is obtained from `dqde` by converting all the double precision constants into the corresponding quadruple precision ones such as `TWOPI = 6.283185307179586476925286766559q0` and modifying the parameters as `MMAx = 4092`.

Table 1. Double precision Fortran 90 subroutine to integrate $s \equiv \int_a^b f(x)dx$ numerically with the relative error tolerance δ by means of the double exponential rule (Takahashi and Mori 1973, 1974; Mori 1985).

```

subroutine dqde(f,a,b,delta,s)
integer MMAX,m
real*8 f,a,b,delta,s,TWOPI,SAFETY,hmax,sdelta,factor,deltah,h0,eph,emh,deltat
real*8 apb,bma,sr,h,sprev,srprev,t,et,ep,em,eppem,xw,xa,wg,fa,fb,fapfb,errt,errh,errd
parameter (TWOPI=6.28318530717958648d0,MMAX=1024,SAFETY=10.d0)
if(delta.gt.1.d-4) then
    hmax=2.75d0+(-log10(delta))*0.75d0
elseif(delta.gt.1.d-6) then
    hmax=3.75d0+(-log10(delta))*0.5d0
elseif(delta.gt.1.d-10) then
    hmax=5.25d0+(-log10(delta))*0.25d0
else
    hmax=6.5d0+(-log10(delta))*0.125d0
endif
sdelta=SAFETY*delta;factor=1.d0-log(sdelta);deltah=sqrt(sdelta);h0=hmax/factor
eph=exp(h0);emh=1.d0/eph;deltat=exp(-emh*factor); apb=a+b;bma=b-a;m=1
sr=f((apb)*0.5d0)*(bma*0.25d0);s=sr*(2.d0*TWOPI);err=abs(s)*deltat;h=2.q0*h0
1 continue
    sprev=s;srprev=sr;t=h*0.5d0
2 continue
    et=exp(t);ep=TWOPI*et;em=TWOPI/et
3 continue
    xw=1.d0/(1.d0+exp(ep-em));eppem=ep+em;xa=bma*xw
    wg=xa*(1.d0-xw);fa=f(a+xa)*wg;fb=f(b-xa)*wg;fapfb=fa+fb
    sr=sr+fapfb;s=s+fapfb*eppem;errt=(abs(fa)+abs(fb))*eppem
    if(m.eq.1) err=err+errt*deltat
    ep=ep*eph;em=em*emh
    if(errt.gt.err.or.xw.gt.deltah) goto 3
    t=t+h
    if(t.lt.h0) goto 2
if(m.eq.1) then
    errh=(err/deltat)*deltah*h0;errd=1.d0+2.d0*errh
else
    errd=h*(abs(s-2.d0*sprev)+4.d0*abs(sr-2.d0*srprev))
endif
h=h*0.5d0;m=m*2
if(errd.gt.errh.and.m.lt.MMAX) goto 1
s=s*h
return;end

```

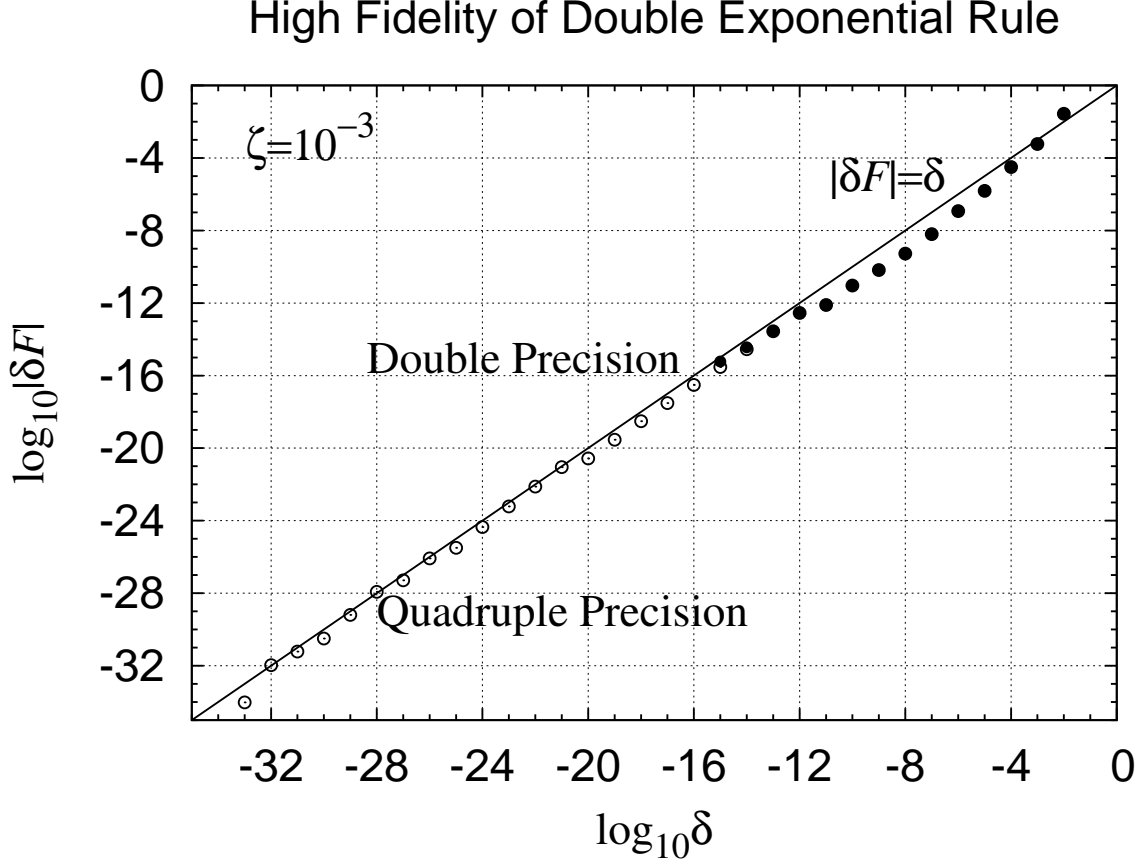


Figure 16. Fidelity of double exponential (DE) rule. Shown are δF , the relative error of the integral $F(\zeta)$ defined in Eq. (C33), obtained by the DE rule. Plotted are the results when $\zeta = 10^{-3}$ as a function of δ , the input relative error tolerance, in a double logarithmic manner. Filled and open circles indicate the results obtained in the double and quadruple precision environments, respectively. The solid straight line shows the line of 100% fidelity, namely when $|\delta F| = \delta$.

C.2. Numerical experiments

In order to show the performance of the implemented Fortran programs, we integrate a test integral defined as

$$F(\zeta) \equiv \int_0^{2\pi} f(\eta, \zeta) d\eta, \quad (\text{C33})$$

where the integrand is expressed as

$$f(\eta, \zeta) \equiv \begin{cases} \ln(\zeta + \sqrt{\eta^2 + \zeta^2}), & (\zeta \geq 0), \\ \ln[\eta^2 / (-\zeta + \sqrt{\eta^2 + \zeta^2})], & (\zeta < 0), \end{cases} \quad (\text{C34})$$

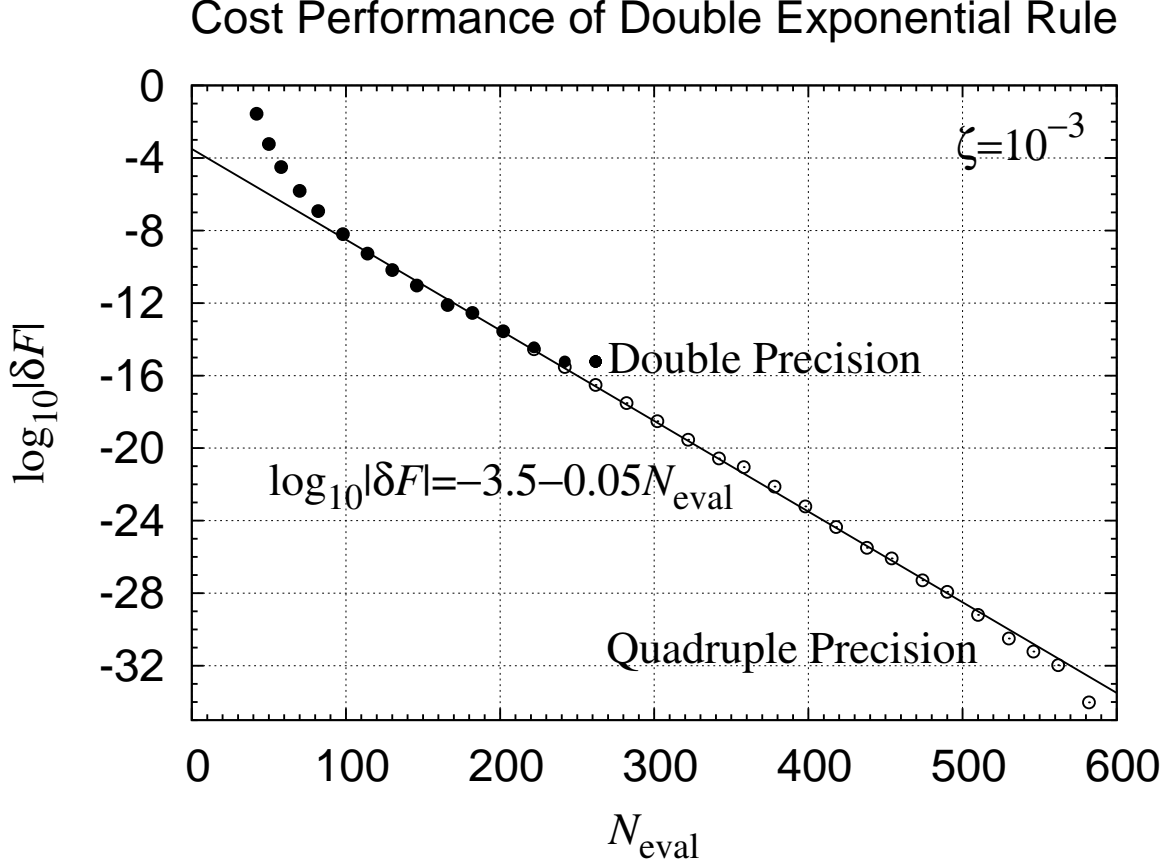


Figure 17. Cost performance of double exponential rule. Same as Fig. 16 but plotted as function of N_{eval} , the number of integrand evaluations. A solid straight line represents the error model function, $\log_{10} |\delta F| = -3.5 - 0.05N_{\text{eval}}$.

This integrand is obtained by simplifying $L(r, \phi, \lambda)$ in the main text such that the integral is analytically computable. Indeed, $F(\zeta)$ is explicitly written in a closed form as

$$F(\zeta) = 2\pi [f(2\pi, \zeta) - 1] + \zeta \ln \left[\left(2\pi + \sqrt{4\pi^2 + \zeta^2} \right) / |\zeta| \right]. \quad (\text{C35})$$

By using the analytical expression, equation (C35), we examined the achieved accuracy and the computational cost of the Fortran programs. First, Fig. 16 illustrates the relation between the achieved integration errors, $|\delta F|$, and the input relative error tolerance, δ . On the other hand, Fig. 17 shows the relation between δF and the computational cost N_{eval} , namely the number of integrand evaluations. These figures indicate a credibility and a good cost performance of the DE rule. Indeed, they are (i) reliable in the sense that the achieved relative error $|\delta F|$ is almost the same as δ ,

Table 2. Double precision Fortran 90 function to compute $\log_{10}(x)$ by conditionally utilizing its type (7,6) relatively minimax rational function approximation in the interval, $0 \leq x \leq 1$, evaluated by Estrin's scheme (Estrin 1960).

```

real*8 function dlog1p(x)
real*8 x,x1,x2,x4,a1,a2,a3,a4,a5,a6,a7,b1,b2,b3,b4,b5,b6
parameter (a1=0.9999999999999999405d0,a2=2.45235728562912886048d0)
parameter (a3=2.17053627298972253249d0,a4=0.83928994566440838378d0)
parameter (a5=0.13520496594993836479d0,a6=0.00682631751459270270d0)
parameter (a7=0.00002291289324181940d0)
parameter (b1=2.95235728562912599232d0,b2=3.31338158247117791600d0)
parameter (b3=1.76186164168333482938d0,b4=0.44976458082070468584d0)
parameter (b5=0.04896199808811261680d0,b6=0.00157389087429218809d0)
if(x.lt.-0.5d0.or.x.gt.1.d0) then
    dlog1p=log(1.d0+x)
elseif(x.ge.0.d0) then
    x1=x
    x2=x1*x1; x4=x2*x2
    dlog1p=x1*(((a1+x1*a2)+x2*(a3+x1*a4))+x4*((a5+x1*a6)+x2*a7)) &
        /(((1.d0+x1*b1)+x2*(b2+x1*b3))+x4*((b4+x1*b5)+x2*b6))
else
    x1=-x/(1.d0+x)
    x2=x1*x1; x4=x2*x2
    dlog1p=-x1*(((a1+x1*a2)+x2*(a3+x1*a4))+x4*((a5+x1*a6)+x2*a7)) &
        /(((1.d0+x1*b1)+x2*(b2+x1*b3))+x4*((b4+x1*b5)+x2*b6))
endif
return; end

```

and (ii) efficient because $|\delta F|$ decreases exponentially when N_{eval} , the computational cost, increases linearly as $\log_{10} |\delta F| = -3.5 - 0.05 N_{\text{eval}}$. From these two figures, we learn that the programs `dqde` and `qqde` are trustable and highly effective.

D. MINIMAX APPROXIMATION OF LOG1P

Let us consider a precise and fast computation of a special logarithm function,

$$\log_{10} p \equiv \ln(1 + x). \quad (\text{D36})$$

It is well known that this defining form suffers from the information loss of one bit or more when $-1/2 < x < 1$. Thus, a specialized program to compute it is added to the standard mathematical libraries in C, C++, and MATLAB. Since no such program is available in Fortran, we present here the minimax approximation of `log1p` by a rational function obtained by `MiniMaxApproximation` command of Mathematica

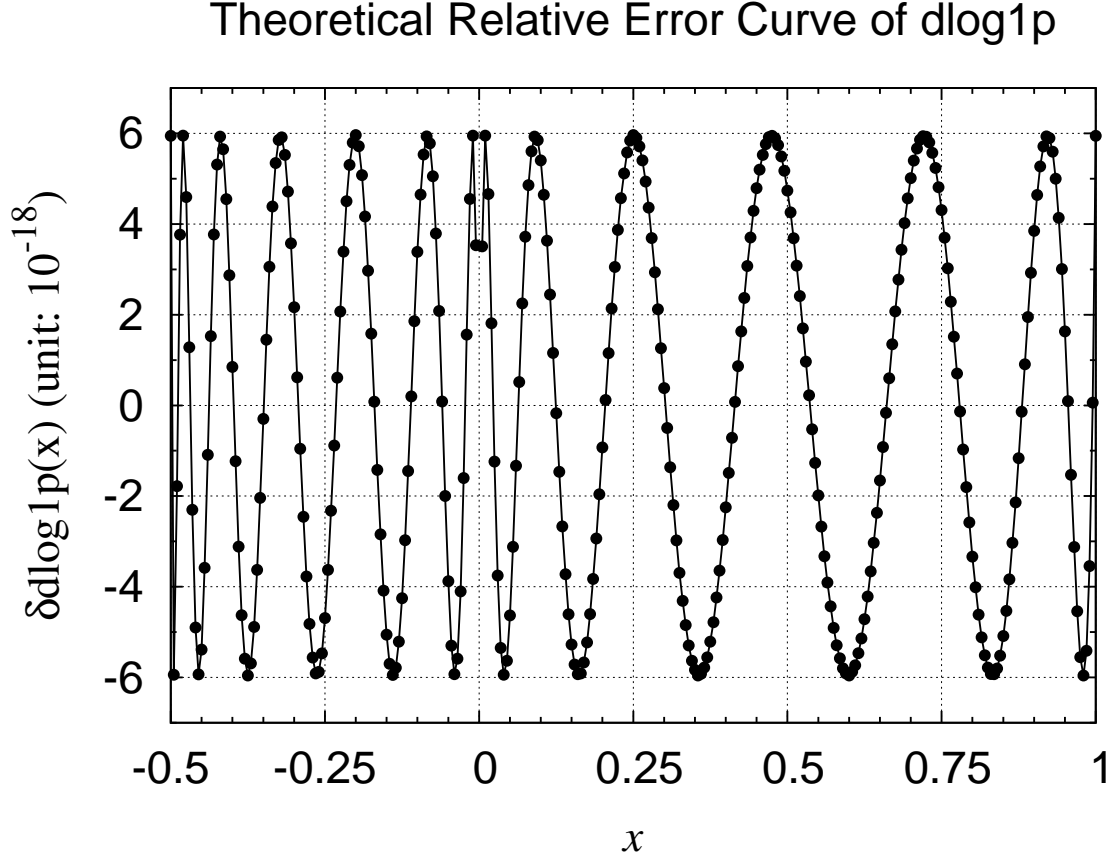


Figure 18. Theoretical relative error curve of dlog1p . Plotted is the relative errors of $\text{dlog1p}(x)$. The errors are defined as $\delta\text{dlog1p}(x) \equiv \text{dlog1p}(x) / \ln(1+x) - 1$ and evaluated in the quadruple precision environment. Obvious is the minimax nature of the relative errors in the interval, $-1/2 \leq x \leq 1$, with the maximum magnitude of relative error as $\approx 6 \times 10^{-18}$.

(Wolfram 2003). The obtained approximation is a type (7,6) rational function written as

$$\text{alog1p}(x) \equiv \frac{\sum_{n=1}^7 a_n x^n}{1 + \sum_{m=1}^6 b_m x^m}, \quad (0 \leq x \leq 1). \quad (\text{D37})$$

By using this approximation, $\text{dlog1p}(x)$ is conditionally constructed as

$$\text{dlog1p}(x) = \begin{cases} -\text{alog1p}(-x/(1+x)), & (-1/2 \leq x < 0), \\ \text{alog1p}(x), & (0 \leq x \leq 1), \\ \ln(1+x), & (\text{otherwise}). \end{cases} \quad (\text{D38})$$

Table 2 shows `dlog1p`, a sample double precision Fortran 90 function using Estrin’s scheme (Estrin 1960) to evaluate the rational function. If the round-off errors are ignored, these approximations are expected to be of the 57 bit relative accuracy as illustrated in Fig. 18. As for the CPU time, we experimentally confirmed that `dlog1p(x)` runs almost the same as the defining form of `log1p(x)` where $\ln(x)$ is provided by the mathematical function library in the problematic argument range, $-1/2 \leq x \leq 1$.

REFERENCES

- Aljbaae, S., Chanut, T.G.G., Carruba, V., Souchay, J., Prado, A.F.B.A., Amarante, A. 2017, Mon. Not. R. Astron. Soc., 464, 3552
- Anderson, E.G. 1976, Rep. Surv. Univ. New South Wales, Unisurv S-14
- Asgharzadeh, M.F., von Frese, R.R.B., Kim, H.R., Leftwich, T.E., Kim, J.W. 2007, Geophys. J. Int., 169, 1
- Bailey, D.H., Jeyabalan, K., Li, X.S. 2005, Exper. Math., 14, 317
- Barnett, C.T. 1976, Geophys., 41, 1353
- Binney, J., Tremaine, S. 2008, Galactic Dynamics (2nd ed.), Princeton Univ. Press, Princeton
- Byrd, P. F., Friedman, M. D. 1971, Handbook on Elliptic Integrals for Engineers and Physicists, 2nd ed., Springer-Verlag, Berlin
- Chandrasekhar, S. 1969, Ellipsoidal Figures of Equilibrium, Yale Univ. Press, Boston (reprinted 1987, Dover Publ.)
- Chandrasekhar, S. 1995, Newton’s *Principia* for the Common Reader, Oxford Univ. Press, Oxford
- Chanut, T.G.G., Aljbaae, S., Carruba, V. 2015 Mon. Not. R. Astron. Soc., 450, 3742
- Chanut, T.G.G., Winter, O.C., Amarante, A., Araujo, N.C.S. 2015 Mon. Not. R. Astron. Soc., 452, 1316
- Chanut, T.G.G., Winter, O.C., Tsuchida, M. 2014 Mon. Not. R. Astron. Soc., 438, 2672
- Chapman, M.E., 1979, J. Geophys. Res., 84, 8B0806
- Conway, J.T. 2015, Celest. Mech. Dyn. Astron., 121, 17
- Du, J., Chen, C., Lesur, V., Lane, R., Wang, H. 2015, Geophys. J. Int., 201, 1977
- D’Urso, M.G. 2013, J. Geodesy, 87, 239
- D’Urso, M.G. 2014a, J. Geodesy, 88, 13
- D’Urso, M.G. 2014b, Celest. Mech. Dyn. Astron., 120, 349
- D’Urso, M.G., Trotta, S. 2015, J. Geodesy, 89, 199
- Dziewonski, A.M., Anderson, D.L. 1981, Phys. Earth Planet. Int., 25, 297
- Estrin, G. 1960, Proc. Western Joint Comput. Conf., 33
- Fahnestock, E.G., Scheeres, D.J. 2006, Celest. Mech. Dyn. Astron., 96, 317
- Fujiwara, A., Kawaguchi, J., Yeomans, D. K., Abe, M., Mukai, T., Okada, T., Saito, J., Yano, H., Yoshikawa, M., Scheeres, D. J., Barnouin-Jha, O., Cheng, A. F., Demura, H., Gaskell, R. W., Hirata, N., Ikeda, H., Kominato, T., Miyamoto, H., Nakamura, A. M., Nakamura, R., Sasaki, S., Uesugi, K. 2006, Science, 312, 1330
- Fukushima, T. 2010, Celest. Mech. Dyn. Astron., 108, 339
- Fukushima, T. 2012a, J. Geodesy, 86, 271
- Fukushima, T. 2012b, J. Geodesy, 86, 745
- Fukushima, T. 2012c, J. Geodesy, 86, 1019
- Fukushima, T. 2013, J. Geodesy, 87, 303
- Fukushima, T. 2014a, Astron. J., 147, 152
- Fukushima, T. 2014b, Appl. Math. Comp., 238, 485
- Fukushima, T. 2014c, Comp. Geosci., 63, 17

- Fukushima, T. 2016a, *Mon. Not. R. Astron. Soc.*, 456, 3702
- Fukushima, T. 2016b, *Mon. Not. R. Astron. Soc.*, 459, 3825
- Fukushima, T. 2016c, *Astron. J.*, 152, 35
- Fukushima, T. 2016d, *Mon. Not. R. Astron. Soc.*, 462, 2138
- Fukushima, T. 2016e, *Mon. Not. R. Astron. Soc.*, 463, 1500
- Fukushima, T. 2017, *Comp. Phys. Comm.*, in printing
- Ganguly, J., Freed, A.M., Saxenac, S.K. 2009, *Phys. Earth Planet. Int.*, 172, 257
- Garcia-Abdeslem, J. 1992, *Geophys.*, 57, 470
- Garcia-Abdeslem, J. 2005, *Geophys.*, 70, J39
- Garcia-Abdeslem, J., Martin-Atienza, B. 2001, *Geophys.*, 66, 1110
- Garmier, R. Barriot, J.-P. 2001, *Celest. Mech. Dyn. Astron.*, 79, 235
- Garmier, R. Barriot, J.-P. 2002, *Geophys. Res. Lett.*, 29, 1231
- Grombein, T., Seitz, K., Heck, B. 2013, *J. Geodesy*, 87, 645
- Hamayun, P., Prutkin, I., Tenzer, R. 2009, *J. Geodesy*, 83, 1163
- Han, J., Shen, W. 2010, *Geosp. Inf. Sci.*, 13, 60
- Heck, B., Seitz, K. 2007, *J. Geodesy*, 81, 121
- Heiskanen, W.A., Moritz, H. 1967, *Physical Geodesy*, Freeman and Co, San Francisco
- Hikida, H., Wiczeorek, M.A. 2007, *Icarus*, 192, 150
- Hirt, C., Kuhn, M. 2014, *J. Geophys. Res. Solid Earth*, 119, 3646
- Hobson, E. W. 1931, *The Theory of Spherical and Spheroidal Harmonics*, Cambridge Univ. Press, Cambridge
- Holstein, H. 2002, *Geophys.*, 67, 1126
- Holstein, H. 2003, *Geophys.*, 68, 157
- Holstein, H., Ketteridge, B. 1996, *Geophys.*, 61, 357
- Holstein, H., Schurholz, P., Starr, A.J., Chakroborty, M. 1999, *Geophys.*, 64, 1434
- Hu, W.D., Scheeres, D.J. 2004, *Planet. Space Sci.*, 52, 685
- Hu, W.D., Scheeres, D.J. 2008, *Chin. J. Astron. Astrophys.*, 8, 108
- Huang, J., Vanicek, P., Pagiatakis, S.D., Brink, W. 2001, *J. Geodesy*, 74, 805
- Jekeli, C. 2007, *Potential Theory and Static Gravity Field of the Earth*, in *Treatise on Geophysics*, 2nd ed. (Schubert, G. ed), Vol. 3, Chapt. 3.02
- Jiang, Y., Baoyin, H. 2016, *Astron. J.*, 152, 137
- Jorda, L. et al. 2016, *Icarus*, 277, 257
- Karcol, R. 2011, *Stud. Geophys. Geodsy*, 55, 21
- Kellogg, O. D. 1929, *Foundations of Potential Theory*, Springer, Berlin
- Kennett, B.L.N. 1998, *Geophys. J. Int.*, 132, 374
- Klees, R. 1996, *J. Geodesy*, 70, 781
- Klees, R., Lehmann, R. 1998, *J. Geodesy*, 72, 530
- Konopliv, A.S., Asmar, S.W., Park, R.S., Bills, B.G., Centinello, F., Chamberlin, A.B., Ermakov, A., Gaskell, R.W., Rambaux, N., Raymond, C.A., Russell, C.T., Smith, D.E., Tricarico, P., Zuber, M.T. 2014, *Icarus*, 240, 103
- Korycansky, D.G. 2004, *Astrophys. Space Sci.*, 291, 57
- Laplace, P.S. 1799, *Traité de Mécanique Céleste*, Tome 1, Chez J.B.M. Duprat, Paris
- Lhotka, C., Reimond, S., Souchay, J., Baur, O. 2016, *Mon. Not. R. Astron. Soc.*, 455, 3588
- Li, X., Gao, A., Qiao, D. 2017, *Astrophys. Space Sci.*, 362, 85
- Li, X., Qiao, D., Cui, P. 2013, *Astrophys. Space Sci.*, 348, 417
- Liu, X., Shan, Z., Li, Y. 2017, *Adv. Space Res.*, 59, 2173
- MacMillan, W.D. 1930, *The theory of the potential*, McGraw-Hill, New York
- Matsuoka, A., Russell, C. T. 2017, *Space Sci. Rev.*, 208, 1
- Miller, J.K., Konopliv, A.S., Antreasian, P.G., Bordi, J.J., Chesley, S., Helfrich, C.E., Owen, W.M., Wang, T.C., Williams, B.G., Yeomans, D.K., Scheeres, D.J. 2002, *Icarus*, 155, 3

- Mori, H. 1985, *J. Comp. Appl. Math.* 12&13, 119
- Moritz, H. 1980, *Advanced Physical Geodesy*, Herbert Wichmann, Karlsruhe
- Müller, T.G., Hasegawa, S., Usui F. 2014, *Publ. Astron. Soc. Japan*, 66, 52
- Müller, T.G., Durech, J., Ishiguro, M., Mueller, M., Kruhler, T., Yang, H., Kim, M.-J., O'Rourke, L., Usui, F., Kiss, C., Altieri, B., Carry, B., Choi, Y.-J., Delbo, M., Emery, J.P., Greiner, J., Hasegawa, S., Hora, J.L., Knust, F., Kuroda, D., Osip, D., Raul, A., Rivkin, A., Schady, P., Thomas-Osip, J., Trilling, D., Urakawa, S., Vilenius, E., Weissman, P., Zeidler, P. 2016, *Astron. Astrophys.*, 599, A103
- Nagy, D. 1966, *Geophys.*, 31, 362
- Nagy, D., Papp, G., Benedek, J. 2000, *J. Geodesy*, 74, 553
- Novak, P., Grafarend, E.W. 2005, *J. Geodesy*, 78, 691
- Okabe, M. 1979, *Geophys.*, 44, 730
- Park, R.S., Konopliv, A.S., Asmar, S.W., Bills, B.G., Gaskell, R.W., Raymond, C.A., Smith, D.E., Toplis, M.J., Zuber, M.T. 2014, *Icarus*, 240, 118
- Paul, M.K. 1974, *Pure Appl. Geophys.*, 112, 553
- Petrovic, S. 1996, *J. Geodesy*, 71, 44
- Pohanka, V. 1988, *Geophys. Prospect*, 36, 733
- Pohanka, V. 1998, *Geophys. Prospect*, 46, 391
- Press W.H., Teukolsky S.A., Vetterling W.T., Flannery B.P. 2007, *Numerical Recipes: the Art of Scientific Computing*, 3rd ed., Cambridge Univ. Press, Cambridge
- Ridders, C.J.F. 1982, *Adv. Eng. Softw.*, 4, 75
- Rosshi, A., Marzari, F., Farinella, P. 1999, *Earth Planet Space.*, 51, 1173
- Roussel, C., Verdun, J., Cali, J., Masson, F. 2015, *Geophys. J. Int.*, 203, 2220
- Scheeres, D.J. 1994, *Icarus*, 110, 225
- Scheeres, D.J., Khushalani, B., Werner, R.A. 2000, *Planet. Space Sci.*, 48, 965
- Scheeres, D.J., Williams, B.G., Miller, J.K. 2000, *J. Guid. Control Dyn.*, 23, 466
- Scheeres, D.J., Ostro, S.J., Hudson, R.S., DeJong, E.M., Suzuki, S. 1998, *Icarus*, 132, 53
- Scheeres, D.J., Ostro, S.J., Hudson, R.S., Werner, R.A. 1996, *Icarus*, 121, 67
- Sebera, J., Bezdek, A., Pesek, I., Henych, T. 2016, *Icarus*, 272, 70
- Shen, W.-B., Deng, X.-L. 2016, *Stud. Geophys. Geod.*, 60, 583
- Singh, B., Gupthasarma, D. 2001, *Geophys.*, 66, 521
- Smith, D.A. 2000, *J. Geodesy*, 74, 414
- Smith, D.A., Robertson, D.S., Milbert, D.G. 2001, *J. Geodesy*, 74, 783
- Takahashi, H., Mori, H. 1973, *Numer. Math.*, 21, 206
- Takahashi, H., Mori, H. 1974, *Publ. RIMS Kyoto Univ.*, 9, 721
- Takahashi, Y., Scheeres, D.J. 2014, *Celest. Mech. Dyn. Astron.* 119, 169
- Takahashi, Y., Scheeres, D.J., Werner, R.A. 2013 *J. Guidance, Control Dyn.*, 36, 362
- Thomas, P.C., Joseph, J., Carcich, B., Veverka, J., Clark, B.E., Bell, J.F.III, Byrd, A.W., Chomko, R., Robinson, M., Murchie, S., Prockter, L., Cheng, A., Izenberg, N., Malin, M., Chapman, C., McFadden, L.A., Kirk, R., Gaffey, M., Lucey, P.G. 2002, *Icarus*, 155, 18
- Tsoulis, D. 2012, *Geophys.*, 77, F1
- Tsoulis, D., Gonindard, N., Jamet, O., Verdun, J. 2009, *J. Geodesy*, 83, 925
- Tsoulis, D., Papanikolaou, T., Vassiliadis, I., Venesis, C. 2012, *J. Geod. Sci.*, 2, 240
- Tsoulis, D., Petrovic, S. 2001, *Geophys.*, 66, 535
- Tsuda, Y., Yoshikawa, M., Abe, M., Minamino, H. 2013, *Acta Astronautica*, 91, 356
- Waldvogel, J. 1979, *J. Appl. Math. Phys.*, 30, 388
- Wang, X.-Y., Li, J.-F., Gong, S.-P. 2014, *Acta Mech. Sinica*, 30, 316
- Wang, X.-Y., Li, J.-F., Gong, S.-P. 2016, *Mon. Not. R. Astron. Soc.*, 455, 3724

- Watanabe, S., Tsuda, Y., Yoshikawa, M.,
Tanaka, S., Saiki, T., Nakazawa, S.
2017 *Space Sci. Rev.*, 208, 3
- Werner, R.A. 1994, *Celest. Mech. Dyn. Astron.*, 59, 253
- Werner, R.A. 1997, *Comp. Geosci.*, 23, 1071
- Werner, R.A., Scheeres, D.J. 1997, *Celest. Mech. Dyn. Astron.*, 65, 313
- Werner, R.A., Scheeres, D.J. 2005, *Celest. Mech. Dyn. Astron.*, 91, 337
- Wild-Pfeiffer, F. 2008, *J. Geodesy*, 82, 637
- Wolfram, S. 2003, *The Mathematica Book*, 5th ed., Wolfram Research Inc/Cambridge Univ Press, Cambridge
- Wu, L. 2016, *Geophys. J. Int.*, 205, 160
- Yu, Y., Baoyin, H. 2012a, *Mon. Not. R. Astron. Soc.*, 427, 872
- Yu, Y., Baoyin, H. 2012b, *Astron. J.*, 143, 160
- Yu, Y., Baoyin, H. 2013, *Astrophys. Space Sci.*, 343, 75
- Yu, Y., Baoyin, H. 2015, *Astrophys. Space Sci.*, 355, 43
- Zhao, Y.-H., Hu, S.-C., Wang, S., Ji, J.-H. 2016, *Chin. Astron. Astrophys.*, 40, 45
- Zuber, M.T., Smith, D.E., Cheng, A.F., Garvin, J.B., Aharonson, O., Cole, T.D., Dunn, P.J., Guo, Y., Lemoine, F.G., Neumann, G.A., Rowlands, D.D., Torrence, M.H. 2000, *Science*, 289, 2097